TURUN
YLIOPISTO
UNIVERSITY
OF TURKU

Reduction of contact losses in metal-semiconductor interfaces via atomic-scale interface research

Mikko Miettinen

TURUN YLIOPISTON JULKAISUJA – ANNALES UNIVERSITATIS TURKUENSIS
SARJA – SER. AI OSA – TOM. 756 | ASTRONOMICA – CHEMICA – PHYSICA – MATHEMATICA | TURKU 2026

TURUN
YLIOPISTO
UNIVERSITY
OF TURKU

REDUCTION OF CONTACT LOSSES IN METAL-SEMICONDUCTOR INTERFACES VIA ATOMIC-SCALE INTERFACE RESEARCH

Mikko Miettinen

TURUN YLIOPISTON JULKAISUJA ANNALES UNIVERSITATIS TURKUENSIS
SARJA SER. AI OSA TOM. 756 | ASTRONOMICA CHEMICA PHYSICA MATHEMATICA | TURKU 2026

University of Turku

Faculty of Science
Department of Physics and Astronomy
Materials Science
Doctoral Programme in Exact Sciences (EXACTUS)

Supervised by

Professor Pekka Laukkanen
Department of Physics and Astronomy
University of Turku
Turku, Finland

Docent Marko Punkkinen
Department of Physics and Astronomy
University of Turku
Turku, Finland

Reviewed by

Professor Mats Göthelid
Division of Light and Matter Physics
KTH Royal Institute of Technology
Stockholm, Sweden

Doctor Jani Oksanen
Department of Neuroscience and
Biomedical Engineering
Aalto University
Espoo, Finland

Opponent

Professor Filip Tuomisto
Department of Physics
University of Helsinki
Helsinki, Finland

ISBN 978-952-02-0555-3 (PRINT)
ISBN 978-952-02-0556-0 (PDF)
ISSN 0082-7002 (PRINT)
ISSN 2343-3175 (ONLINE)
Painosalama, Turku, Finland, 2026

UNIVERSITY OF TURKU
Faculty of Science
Department of Physics and Astronomy
Materials Science
MIETTINEN MIKKO: Reduction of contact losses in metal-semiconductor interfaces via atomic-scale interface research
Doctoral dissertation, 66 pp.
Doctoral Programme in Exact Sciences (EXACTUS)
February 2026

ABSTRACT

This doctoral thesis investigates treating and modification of silicon and gallium nitride surfaces and their interaction with metals in metal-semiconductor contacts. The key factor behind the experiments and results in this thesis is the utilization of ultra-high vacuum conditions in preparation and characterization of the materials. The interface between the metal and the semiconductor determines the type and quality of the formed contact, which is why understanding and developing of it is crucial to reduce electrical losses and enhance the efficiency and life span of semiconductor devices.

In this work, the surfaces of n-type silicon and p-type gallium nitride were investigated. The surfaces were treated with wet chemistry and by heating and exposing the surfaces to gasses in ultra-high vacuum. The surfaces were measured with scanning tunneling microscopy/spectroscopy, x-ray photoelectron spectroscopy, and low-energy electron diffraction. The metal-semiconductor contacts were characterized by measuring the contact resistivity, and with gallium nitride, the interface was also investigated with synchrotron radiation x-ray photoelectron spectroscopy.

The results show that i) nickel forms a silicide with the silicon already at the room temperature but the electrical properties of the said silicide depend on the silicon surface treatments, and the doping concentration has a clear impact on the path of the current flow between the contacts; ii) by heating the Ni-GaN interface in ultra-high vacuum, the gallium diffuses to the nickel layer and the vacancies created in the interface act as a route for the charge carries to tunnel through the potential barrier, leading to an ohmic contact; iii) by treating silicon devices, which already contained metal contacts, in ultra-high vacuum, the quality of the surface can be improved, and hence it is possible to improve the performance of devices made from silicon.

KEYWORDS: Ultra-high vacuum, contact losses, surface treatment, semiconductor interfaces

TURUN YLIOPISTO
Matemaattis-luonnontieteellinen tiedekunta
Fysiikan ja tähtitieteen laitos
Materiaalitiede
MIETTINEN MIKKO: Reduction of contact losses in metal-semiconductor interfaces via atomic-scale interface research
Väitöskirja, 66 s.
Eksaktien tieteiden tohtoriohjelma (EXACTUS)
Helmikuu 2026

TIIVISTELMÄ

Tämä väitöskirja käsittelee pii- ja galliumnitridipintojen käsittelyä ja muokkausta, sekä niiden vuorovaikutusta metallien kanssa metalli-puolijohdekontakteissa hyödyntäen tyhjiötekniikan menetelmiä. Väitöskirjan kokeiden ja tulosten yhdistävä tekijä on ultrasuurtyhjiöolosuhteiden käyttäminen materiaalien käsittelyssä ja karakterisoinnissa. Metallin ja puolijohteen välinen rajapinta määrittää syntyvän kontaktin tyypin ja laadun, jolloin sen ymmärtäminen ja kehittäminen ovat avainasemassa sähköisten häviöiden vähentämisessä ja puolijohdelaitteiden tehokkuuden ja käyttöiän parantamisessa.

Työssä tutkittiin n-tyyppisen piin ja p-tyyppisen galliumnitridin pintoja. Pintoja käsiteltiin märkäkemialla sekä ultrasuurtyhjiössä lämmittämällä ja altistamalla kaasuille, ja metallin kanssa muodostettuja rajapintoja käsiteltiin niin ikään ultrasuurtyhjiössä lämmittämällä ja altistamalla kaasuille. Pintoja tutkittiin tunnelointimikroskopialla ja -spektroskopialla, röntgenviritteisellä fotoelektronispektoskopialla sekä matalaenergisellä elektronidiffraktiolla. Metalli-puolijohdekontakteja karakterisoitiin mittaamalla kontaktiresistiivisyyttä, ja galliumnitridin tapauksessa rajapintaa tutkittiin myös synkrotronilähteisellä röntgenviritteisellä fotoelektronispektroskopialla.

Väitöskirjan tutkimukset osoittavat, että i) nikkeli muodostaa piin kanssa silisidin jo huoneenlämmössä, mutta sen sähköiset ominaisuudet riippuvat piin pintakäsittelystä, ja piristyskonsentraatio vaikuttaa suuresti virran reittiin kontaktien välissä; ii) Ni-GaN rajapintaa lämmitettäessä ultrasuurtyhjiössä gallium diffusoituu nikkelikerrokseen ja rajapintaan syntyvät vakanssit aiheuttavat varauksenkuljettajille reitin tunneloitua potentiaalivallin läpi, johtaen oomiseen kontaktiin; iii) ultrasuurtyhjiössä tehtävillä käsittelyillä on mahdollista muokata piilaitteiden, joissa on jo metallikontaktit, ominaisuuksia ja täten parantaa niiden suorituskykyä.

ASIASANAT: Ultrasuurtyhjiö, kontaktihäviöt, pintakäsittely, puolijohderajapinnat

Acknowledgements

This work was carried out in the Materials Research group of the Department of Physics and Astronomy of the University of Turku. First, I want to thank my main supervisor, Professor Pekka Laukkanen, who has provided me with invaluable support and help all the way from my summer internship in the lab in 2020. I could not have hoped for a more approachable, supportive, and positive main supervisor. Also, a great thanks goes to Dr. Marko Punkkinen for supporting me as my second supervisor as well as to Prof. Kalevi Kokko for being the director of this work.

It was a pleasure to work with people in the Materials Research group. I thank Dr. Zahra (Elmira) Jahanshah Rad for all the help and thorough discussions, and I especially thank you for your trust and for giving me the possibility to continue working together in the semiconductor industry. Many thanks to Juha-Pekka Lehtiö for teaching and encouraging me to work with the laboratory equipment, as well as providing valuable insights to my research. I also thank Johanna Laaksonen, Dr. Masoud Ebrahimzadeh, Valtteri Alitupa, Dr. Antti Lahti, and Dr. Mikael Santonen for all the help along the way.

In addition to our group members, I thank Dr. Sari Granroth for all the help and advice. I also thank Dr. Risto Punkkinen for providing insight and support with the electrical measurements. In addition, thanks to all the collaborators with whom I had the opportunity to work with.

I thank my pre-examiners Prof. Mats Göthelid and Dr. Jani Oksanen for their helpful comments. I also thank Prof. Filip Tuomisto for being my opponent. In addition, I am grateful for the financial support from the Research Council of Finland, the University of Turku Graduate School, the Emil Aaltonen Foundation, and the Department of Physics and Astronomy.

Last but certainly not least, I express my deepest gratitude to my family and friends. I thank my family for all the encouragement, support and love while making my way to this point. I could not have asked for more. And to my dear Matilda, thank you for your love and being there for me.

10.2.2026
Mikko Miettinen

Table of Contents

Acknowledgements . . . . . **v**

Table of Contents . . . . . **vi**

Abbreviations . . . . . **viii**

List of Original Publications . . . . . **ix**

1 Introduction **1**

2 Principles of semiconductors and interfaces **2**
2.1 Basics of semiconductors 2
2.1.1 Basics of crystal structure 2
2.1.2 Electrical properties of semiconductors 4
2.1.3 Semiconductor materials 6
2.2 Surface properties of semiconductors 7
2.3 Metal-semiconductor contacts 9
2.3.1 Device examples 11

3 Experimental methods **14**
3.1 Ultra-high vacuum (UHV) 14
3.2 Preparing the semiconductor surface 16
3.2.1 Wet chemistry 16
3.2.2 UHV treatments 17
3.3 Surface characterization techniques 18
3.3.1 X-ray photoelectron spectroscopy 18
3.3.2 Low-energy electron diffraction 22
3.3.3 Scanning tunneling microscopy/spectroscopy 23
3.4 Specific contact resistivity measurements 26
3.4.1 Sputter deposition 27
3.4.2 Contact patterning 28

4 Summary of publications **29**

4.1 Effects of Ultra-High Vacuum Treatments on n-Si Contact Resistivity 29
4.2 Surface Properties of p-GaN and Formation of Nickel Metal Contacts 30
4.3 Potential of ultrahigh-vacuum based surface treatments on silicon technology 31

List of References **33**

Original Publications **39**

Abbreviations

CBM	Conduction band maximum
CMOS	Complementary metal-oxide-semiconductor
DIW	De-ionized water
FCC	Face-centered cubic
H_2O_2	Hydrogen peroxide
H_2SO_4	Sulfur acid
HCl	Hydrochloric acid
HCP	Hexagonal close-packed
HF	Hydrofluoric acid
NHO_3	Nitric acid
IV	Current-voltage
KOH	Potassium hydroxide
LEED	Low-energy electron diffraction
MIGS	Metal-induced gap states
MOSFET	Metal-oxide-semiconductor field-effect transistor
MOVPE	Metal organic vapor phase epitaxy
SR-XPS	Synchrotron radiation x-ray photoelectron spectroscopy
STM	Scanning tunneling microscopy
STS	Scanning tunneling spectroscopy
TLM	Transmission length method
UHV	Ultra-high vacuum
VBM	Valence band minimum
XPS	X-ray photoelectron spectroscopy

List of Original Publications

This dissertation is based on the following original publications, which are referred to in the text by their Roman numerals:

I **M. Miettinen**, E. Vuorinen, J.-P. Lehtiö, Z. Jahanshah Rad, R. Punkkinen, M. Kuzmin, J. Järvinen, V. Vähänissi, P. Laukkanen, H. Savin, K. Kokko. *Effects of Ultra-High Vacuum Treatments on n-type Si Contact Resistivity*. Applied Surface Science, 2025; 695: 162790.

II **M. Miettinen**, V. Nuutila, Z. Jahanshah Rad, M. Ebrahimzadeh, A. Ruokonen, R. Punkkinen, J.-P. Lehtiö, M. Punkkinen, P. Laukkanen, K. Kokko, H. Savin, W. Wang. *Surface Properties of p-GaN and Formation of Nickel Metal Contacts.* Advanced Materials Interface, 2025; 12: 200163.

III Z. Jahanshah Rad, **M. Miettinen**, R. Punkkinen, P. Suomalainen, M. Punkkinen, P. Laukkanen, K. Kokko. *Potential of ultrahigh-vacuum based surface treatments in silicon technology.* Microelectric Engineering, 2025; 300: 112382.

1 Introduction

Semiconductors are the basis for all modern electronics and communication. Since the invention of a planar silicon transistor in 1959, the number of components in one chip has increased and increased in a manner known as Moore's law. A well known feature of Moore's law is that as the number of components increases in one chip, the feature size, that is, the lithography line width of one component decreases [1]. The reduction in feature size also leads to an increased role of the semiconductor surfaces and interfaces [2].

Semiconductor devices are dependent on metal-semiconductor contacts, which provide the connection of the devices to the outer world, and problems in the contacts hinder the device performance. For example, in complimentary metal-oxide-semiconductor (CMOS) devices, contact resistance is becoming a more dominant part of the total resistance of the device as the feature size decreases [3]. As another example, in solar cells, harmful recombination of charge carriers occurs in poor quality contacts, decreasing the current collected from the solar cell [4]. To further improve the understanding and performance of the metal-semiconductor interfaces, the interfaces and the semiconductor surfaces before and after the metal deposition need to be studied further.

In this work, the surfaces of silicon and gallium nitride were investigated as well as their interaction with metal contacts and the resulting contact resistivities. The surfaces were treated using wet chemistry for cleaning and passivation of the surfaces, and the wet chemical treatments were often combined with ultra-high vacuum treatments. In ultra-high vacuum, the surfaces were treated by heating the samples and exposing them to different gasses. Ultra-high vacuum was also utilized in characterization and annealing of the metal-semiconductor contacts.

Chapter 2 gives a brief theoretical insight on the properties of semiconductors and metal-semiconductor contacts as well as device examples. In Chapter 3 all the experimental methods utilized in this work are introduced. Finally, in Chapter 4 a summary and main findings of each article I-III associated with this thesis are presented.

2 Principles of semiconductors and interfaces

The key for developing modern semiconductor devices and solutions is understanding the properties of semiconductor surfaces and the interfaces they form with other materials. A single device can contain multiple interfaces (e.g. semiconductor-metal, semiconductor-oxide, and sidewalls of chip) that each have individual properties, and thus individual impact on the device performance. This chapter introduces some basic properties of semiconductors, their surfaces, and interfaces they form with metals.

2.1 Basics of semiconductors

2.1.1 Basics of crystal structure

The ideal crystalline structure of a material is formed from a lattice and a basis. The basis is the smallest building block that forms the material crystal, and the lattice is the mathematical point construction in which the basis is attached. In this case, the basis is a group of atoms, and only one basis can be attached to one lattice point. The lattice is defined by using vectors $\mathbf{a_1}$, $\mathbf{a_2}$ and $\mathbf{a_3}$, and a position of a certain atom can be noted as

$$\mathbf{r} = u_1\mathbf{a_1} + u_2\mathbf{a_2} + u_3\mathbf{a_3}, \tag{1}$$

where u_x are arbitrary integers. This is also the notation to define the Bravais lattice: an infinite array of points that are arranged and oriented in a way that it looks identical despite the direction where the array is observed. The primitive cell is the smallest cell that can be used to fill the lattice space, and single vectors $\mathbf{a_1}$, $\mathbf{a_2}$ and $\mathbf{a_3}$ – also called primitive axes – form it. The primitive cell always has one lattice point. By using these axes, different crystal structures can be formed [5; 6]. Since two different materials were used in this thesis, their crystal structures are introduced.

The diamond structure is formed from the face-centered cubic (FCC) structure with a basis of two atoms. FCC is a cubic structure in which the cube has atoms in its corner and in the middle of it's faces. In contrast to a regular FCC structure, the diamond structure has additional atoms placed at $\mathbf{a_1}/4 + \mathbf{a_2}/4 + \mathbf{a_3}/4$ position from each atom in the FCC structure. Since only four additional atoms are inside

the same unit cell, the diamond structure, in fact, consists of two FCC structures, interpenetrating each other with a displacement of 1/4 in all three dimensions [7]. The diamond structure is represented in Figure 1.

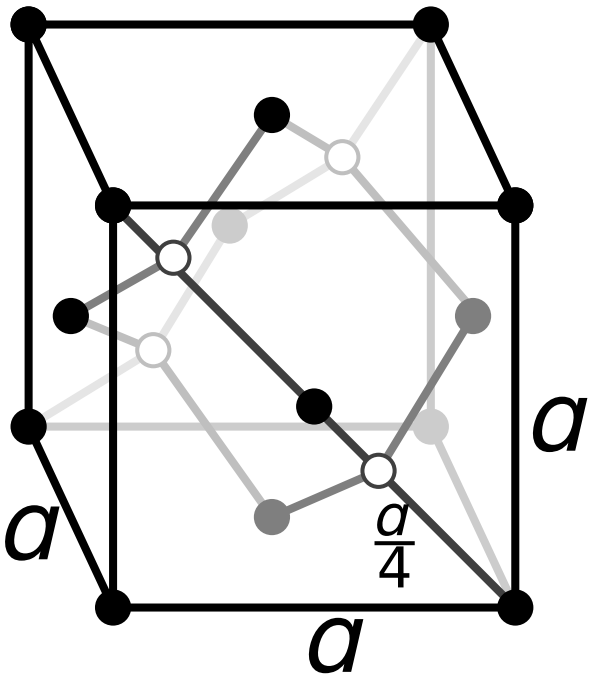

Figure 1. The diamond crystal structure. [8]

While the diamond consists of two interpenetrating FFC structures, the wurtzite structure consists of two hexagonal close-packed structures (HCP) consisting of different atoms. In HCP, each atom is connected to six other atoms, forming layer A. Because stacking the atoms on top of each other is not stable, a second layer B consisting of three atoms is added by connecting each of the layer B atoms with three atoms in layer A. Then an additional layer A is placed right over the bottom A layer atoms. By repeating, ABABAB... structure is achieved. HCP has two lattice parameters, a and c, of which the parameter a describes the distance between two atoms in layer A and B, and the parameter c the distance between two layers of A. In the wurtzite structure, two interpenetrating HCPs are displaced from each other by $3/8c$. [9]. The wurtzite structure is represented in Figure 2.

Real space periodic lattice also has a periodic potential. This means that a potential in point r is the same as in point $r+R$, where R is any Bravais lattice vectors. From this periodicity of potential, we can have

$$\mathbf{G} = n_1\mathbf{A_1} + n_2\mathbf{A_2} + n_3\mathbf{A_3}, \tag{2}$$

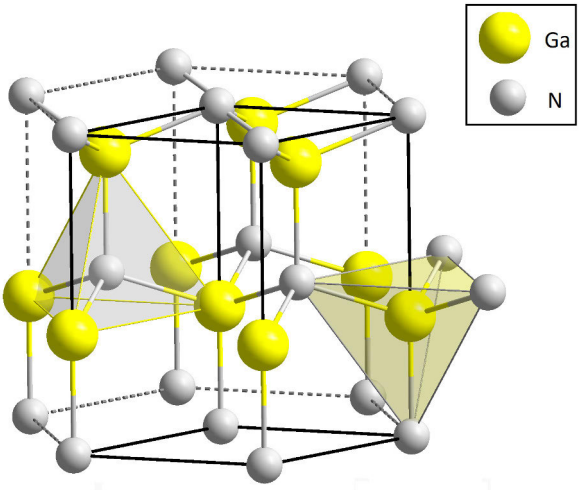

Figure 2. The wurtzite crystal structure of GaN structure with highlighted Ga and N atoms. [10]

where n_y are arbitrary integers and $\mathbf{A_j}$ are vectors which are defined by

$$\mathbf{a_i} \cdot \mathbf{A_j} = 2\pi\delta. \tag{3}$$

This relationship leads to the concept of reciprocal lattice, which is constructed by the vectors in $\mathbf{G}$. The reciprocal lattice lies in *k* space (i.e. 1/m space), which is also periodic. The primitive unit cell of *k* space is called the first Brillouin zone, and Brillouin zone is also later used to describe the energy bands of semiconductors. [11]

2.1.2 Electrical properties of semiconductors

A semiconductor is defined as a material for which the resistivity is highly dependent on the temperature. In the absolute zero point, the semiconductor behaves as a perfect insulator, and the resistivity decreases as the temperature increases. At room temperature, the resistivity of the semiconductor is between 10^{-2} and 10^{9} ohm·cm [5]. The reason for this lies in the band structure: electrons in the highest occupied electrical state, the valence band, can thermally excite to the lowest unoccupied electrical state, the conduction band, but this requires the temperature to be over 0 K. In comparison, with metals the bands overlap, resulting in conductance at 0 K as well, and with insulators the band gap is so large that the thermal excitation from the valence band to the conduction band is hardly probable. The separation in energies between the valence and conduction bands is called the band gap, and in the band gap between the valence and conduction bands lies a Fermi level [6]. The band gap can be either direct or indirect, meaning that the valence band maximum (VBM) and conduction band minimum (CBM) can be located in the same or separate positions

in the $\boldsymbol{k}$ space. This is demonstrated in Figure 3. Since the lattice is considered periodic, the x-axis is presented with symmetry points of the first Brillouin zone in the $\boldsymbol{k}$ space along the wavevector $\boldsymbol{k}$, and they refer to certain points in the reciprocal lattice. [12; 13].

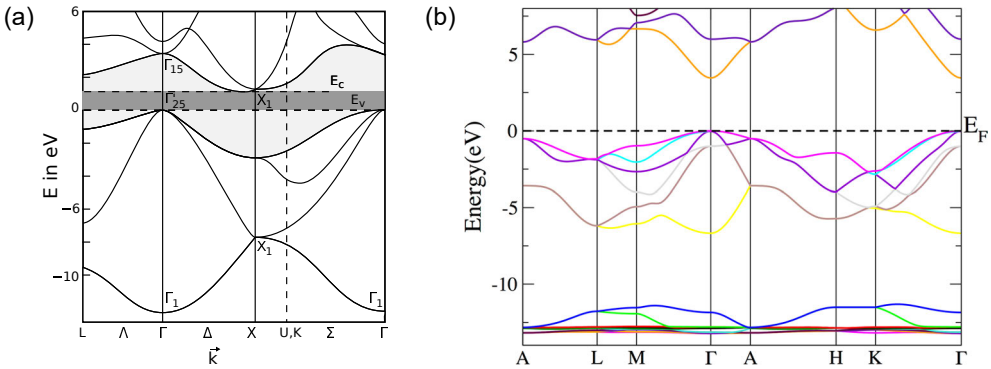

Figure 3. An example of (a) indirect [14] and (b) direct band gap [15] from Si and GaN, respectively.

The directness of the band gap has a role in determining to which application the semiconductor is suitable for: for example, light-emitting diodes (LEDs) require a direct band gap material. With direct band gap material, the electron can excite straight from the VBM to the CBM with the energy it receives - provided that the received energy is larger than the band gap. At some point, depending on the carrier lifetime, the electron recombines back to the valence band. As the charge carriers recombine, an amount of energy equivalent to the band gap is released. In the direct band gap, the energy is released as a photon, making it radiative recombination and hence emitting light. With the indirect band gap, the electron doesn't only require energy to excite to the conduction band, but also momentum, i.e., phonon, so that it can move in $\boldsymbol{k}$ space. However, if the energy of the photon is larger than the band gap, the conduction band structure has energy level to which the electron can excite directly. Since the conservation of momentum is required, for indirect band gap materials the radiative the recombination is highly unlikely, as the energy is released as a phonon transferring the momentum and the energy to the lattice, heating the material. [16]

Band gap of the semiconductor itself can not be altered, as it is based on the material properties. However, the band structure can be altered by doping, i.e., deliberately introducing impurity atoms to the material with different electron structure. The change in the band structure depends on what kind of impurity atoms are introduced to the material. If the impurity atoms have one additional electron compared to the atoms in the lattice, the material becomes n-type and an additional empty level is created below the CBM, between it and the Fermi level. This extra electron

level is called a donor state. If the impurity atoms have one electron less, the material becomes p-type, and an additional electron level is created above the VBM, between it and the Fermi level. This level is called an acceptor state. These states increase, among other things, the conductivity of the material and opens possibilities to make devices by combining n- and p-type materials (see 2.3.1) [17]. However, there are maximum values for effective dopant concentrations depending on the material, due to issues in dopant atom solubility, dopant activation and compensating doping [18; 19; 20].

While deliberately introducing impurities to the lattice adds beneficial doping states to the band gap, not all states in the band gap are desirable. Defects, contamination and unwanted impurities create unwanted energy levels, trap states, to the band gap, which hinder the electrical performance of the material. The trap states can act as a recombination centers, resulting in unwanted recombination. In applications where the charge carrier flow to the outer circuit is required, the unwanted recombination hinders the device efficiency. Trap states in the band gap caused by the issues in the lattice are called deep states, while trap states caused by the surface contaminants and defects are called surface states (see more in 2.2).

2.1.3 Semiconductor materials

Silicon

Silicon is a group IV elemental semiconductor with a diamond crystal structure with a lattice constant of 5.4311 Å. It has an indirect band gap of 1.12 eV [21]. Silicon can be doped with boron to produce p-type silicon or with antimony, arsenic, or phosphorus to produce n-type silicon [22]. N-type silicon used in this thesis was doped with phosphorus.

A common way to produce crystalline silicon is the Czochralski (Cz) method: polycrystalline blocks are melted in a crucible, and a seed crystal is placed into the molten mass. The seed crystal is raised slowly from the mass while the crucible rotates in the clockwise direction and the seed crystal to counterclockwise direction. Slow rise speed and rotation are used to ensure a uniform distribution of atoms and higher crystal quality [23].

Silicon is the most used semiconductor material in the world. Compared to the other common elemental semiconductor, germanium, it has a higher breakdown electric field and a larger band gap, which makes it capable of operating in a higher temperature range without issues caused by the intrinsic conductivity. Silicon is also the second most common material on the Earth, making it easily available and cheap [12]. Silicon is used in, for example, solar cells, photodetectors, and transistors [24].

Gallium Nitride

Gallium nitride is a wide band gap III-V compound semiconductor with a wurtzite crystal structure. Due to the wurtzite structure, GaN has two lattice parameters, a and c, which have values of 3.188 Å and 5.185 Å, respectively [25].

GaN has a band gap of 3.39 eV, which makes it a superior material for power electronics compared to silicon: a higher band gap enables a higher electric field tolerance. Higher electric field tolerance enables smaller components, which decreases the switching time. A higher electric field also means a higher current density, thus decreasing the switching time even further. The leakage current is smaller in high band gap materials, as less charge carriers are generated in the depletion region. These properties make GaN more feasible for, e.g., high-frequency applications compared to elemental semiconductors [26]. Moreover, GaN is the main material for white LEDs [27]. Typical dopants for GaN are silicon and magnesium for n- and p-type doping, respectively [28].

Gallium nitride can be grown by using wither molecular beam epitaxy (MBE) or metal organic chemical vapour deposition (MOCVD). The material used in this thesis was grown using a vertical flow MOCVD, depositing GaN layers on a sapphire substrate. The method utilizes a hot reactor chamber, generally above $1000\,^{\circ}\mathrm{C}$, in which the precursor gases react with each other. For GaN growth, trimethylgallium ($Ga(CH_3)_3$) and ammonia (NH_3) are used. Doping is achieved by adding a dopant precursor to the gas mix. For Si, silane (SiH_4) or disilane (Si_2H_6) is used, and for Mg, cyclopentadienyl magnesium $(C_5H_5)_2Mg$ is used [28].

2.2 Surface properties of semiconductors

While the bulk is well defined and generally follows a periodic and ordered structure, the surface is much more complicated. The surface is created by broken bonds pointing towards vacuum, and these bonds are called dangling bonds. The existence of dangling bonds makes the surface structure more energetically unfavorable, which leads to different surface atom arrangements due to relaxation or reconstruction [29; 30].

The surface is considered to be relaxed if the surface unit cell is similar with the bulk. The horizontal placement of atoms stays the same, but the vertical changes so that there is a displacement, keeping the 2D Bravais lattice, and thus the 2D translational symmetry the same. The vertical change means that the surface atoms lie closer to the next atom layer than they would be in the bulk. This is most common in metals, but is also seen in semiconductors such as GaAs. Reconstruction, on the other hand, means that the unit cell is different from the bulk. In reconstruction, the dangling bonds form new bonds with adjacent atoms and the surface atoms rearrange by moving closer to each other, hence alternating the 2D Bravais lattice. This

is common, especially in the tetrahedrally bonded semiconductors due to the strong directionality of the bonds between the atoms. [31; 32]

The reason for a semiconductor surface to form a reconstruction is the degenerate ground states, meaning a higher energy (inner energy) related to the danging bonds. In other words, a surface reconstruction decreases the total energy of the material. With dangling bonds, there is only one electron per dangling bond, although the bond could accommodate two electrons. By pairing two surface atoms symmetrically, i.e., creating a dimer, half of the dangling bonds are saturated, but half of them are still there, meaning that there are half-filled electron states which are of the same energy. By breaking the symmetry, the lower electron state is filled and the degeneracy is lifted. This is also called the Jahn-Teller effect or theorem. In the case of Si(100), the asymmetry is achieved by partial transfer of an electron from one atom to the other in the dimer, alternating the bond angle and creating a buckled dimer, i.e., the other atom in the dimer is higher than the other one. With some semiconductors, such as the GaAs mentioned earlier, the surface relaxes rather than reconstructs due to the electrostatic neutrality of the surface: the surface has one cation and one anion in the unit cell, hence there are two dangling bonds and two electrons, and no degeneracy is created [31; 32]. In reality, to achieve the reconstruction on the semiconductor surface, the surface needs to be annealed. A temperature as low as $300\,^{\circ}\mathrm{C}$ can be sufficient [33]. Unfortunately, reconstruction can be held for a long time only in vacuum.

Although the reconstruction provides lower energy for, e.g., silicon surface, it's not stable in ambient. In fact, in room temperature in an ambient atmosphere, surface atoms bond to other materials such as oxygen, carbon, and hydrogen due to surface reactivity [34; 35]. Most importantly, the surface spontaneously forms an amorphous native oxide of which growth is self-limiting. Again, the surface-related energy decreases by forming bonds with oxygen, and the native oxide protects the crystal from further contaminants. It is also possible to grow amorphous thermal silicon oxide, which can be controlled more precisely, and it has historically been one of the cornerstones of metal-oxide-semiconductor devices: it is thermodynamically stable, has good interfacial bonding properties, and is a good insulator. The downside is the possibility of it acting as a diffusion path for contaminants, especially metal ions, to the semiconductor crystal, causing degradation in metal-oxide-semiconductor devices [35; 36; 37].

The oxide layer can be removed and the surface can be cleaned with, for example, wet chemistry [38]. After this, the surface is rough and full of dangling bonds. Roughness and dangling bonds are known to cause surface states to the band gap [39; 40]. The said features can also be detrimental to the quality of the formed interface when an additional material layer is deposited on top of the surface [41]. The surface and interfacial states are harmful states in the band gap that are detrimental to the performance of a semiconductor device. They can cause a decrease in electron

drift mobility, leakage current, hinder solar cell performance, and cause Fermi level pinning [31; 41; 42; 43].

Surface roughness and dangling bonds as well as interface issues can be improved by surface treatments. One of the classic ways to improve the surface is passivation. The passivation method depends on the targeted semiconductor material, but generally the passivation can be done using wet chemical or gaseous treatment. An additional way is to grow a thin non-reactive layer on top of a clean surface. For example, with silicon, the most typical passivation agent is hydrogen, which can be applied by using hydrofluoric acid (HF) solution, hydrogen gas or hydrogen plasma. The hydrogen bonds with the dangling bonds, decreasing the states created by them. In addition, the hydrogen passivation prevents the formation of native oxide for a limited duration [44; 45; 46]. Hydrogen isn't an universal passivation agent, and with, for example, III-V semiconductors it doesn't provide the desired passivation. With these semiconductors, passivation can be achieved by depositing a thin high-κ layer, a Si layer, plasma treatments or sulfur based treatments. Sulfur based treatments are closest to hydrogen passivation with HF in Si, since they remove the native oxide and sulfur bonds to the surface, leading to passivation [47].

2.3 Metal-semiconductor contacts

Metal-semiconductor interfaces are a key component in semiconductor devices. They act as a gate for the charge carriers to move in to the device or out from there. The role of this interface increases continuously as the device size decreases, as the surface properties, in general, also become more dominant. There are two main types of contacts that form between a metal and a semiconductor: Schottky and ohmic contacts.

In an ideal case, the type of formed contact is determined by the work functions of the semiconductor ϕ_S and the metal ϕ_M. The work function describes the potential difference between the Fermi level and the vacuum, i.e. how much kinetic energy the electron needs to escape from the Fermi level to free space at 0 K. When metal and semiconductor are brought into contact, their Fermi levels align, causing band bending and a potential barrier (also called Schottky barrier) formation. The barrier height is

$$\phi_B = \phi_M - \chi, \tag{4}$$

where χ is the electron affinity of the semiconductor, meaning the potential difference between the bottom of the conduction band and the vacuum [48]. Schottky contacts present an asymmetric current-voltage (IV) behavior. With forward bias voltage, the potential barrier height on the semiconductor side decreases according to the applied forward bias, increasing the current flow from the semiconductor to the metal in an exponential manner. With reverse bias, the potential barrier height on

the semiconductor side increases, making the current flow from the semiconductor to the metal minimal. Hence, the contact is rectifying, meaning that it lets current through with forward bias but practically blocks the current flow on reverse bias [24].

Ohmic contacts, on the other hand, have linear IV behavior following the Ohm's law. With ohmic contact, there isn't similar potential barrier between the semiconductor and the metal, but the bands bend in such a manner that the current can flow straight from the semiconductor to the metal or vice versa. An ideal ohmic contact has a negligible contact resistance, and the voltage drop is minimal compared to that of the actual active part of the device. Since resistance is property of an actual contact rather than an interface junction, the quality of ohmic contacts is usually evaluated using specific contact resistivity ρ_c. To achieve sufficiently low ρ_c, ideally the semiconductor material must have a high doping concentration, and the two materials forming the contact must have such work functions that the potential barrier is as small as possible. If both doping concentration and barrier height are high, it is possible that a contact, which in principle would be a Schottky contact, actually behaves like an ohmic one due to tunneling of carriers through the barrier. [49]

With the n-type semiconductor, the contact will be ohmic if $\phi_M < \phi_S$ and Schottky if vice versa. With the p-type semiconductor, the contact will be ohmic if $\phi_M > \phi_S$ and Schottky if vice versa. The illustration of interface band structure is presented in Figure 4.

However, in reality, the contact type can not be predicted with just the measured work functions, as they are bulk properties and the surfaces usually have different work functions because of defects, dangling bonds, and contaminants. These features can create interfacial states in the band gap at the metal-semiconductor interface. A high amount of these interfacial states may lead to Fermi level pinning, in which the Fermi level is stuck at some energy where it initially would not be, resulting in a Schottky contact even though, based on work functions, the contact should be ohmic [24; 48; 50].

The contact metal can also contribute to the interfacial states. The origin of extra states in the band gap is explained with metal-induced gap states (MIGS). In vacuum, the wavefunctions of the electrons in the metal decay to the vacuum, but when placed in contact with a semiconductor, the decaying wavefunction tails extend over the interface to the semiconductor. In the energy range where the top of the conduction band of the metal overlaps with the semiconductor band gap, a continuum of states appears. At the same time, semiconductor induced, bulk like states appear on the metal side of the interface. These states affect the Schottky barrier height and make predicting the type of contact more difficult. [51]

Not only do the mentioned issues affect the contact type, they also generally hinder the performance of the said contacts even if the contact type is the one that was desired. For example, with Schottky contacts, the interfacial states generate a higher leakage current, that is, unwanted current flow in the off-state, leading to parasitic

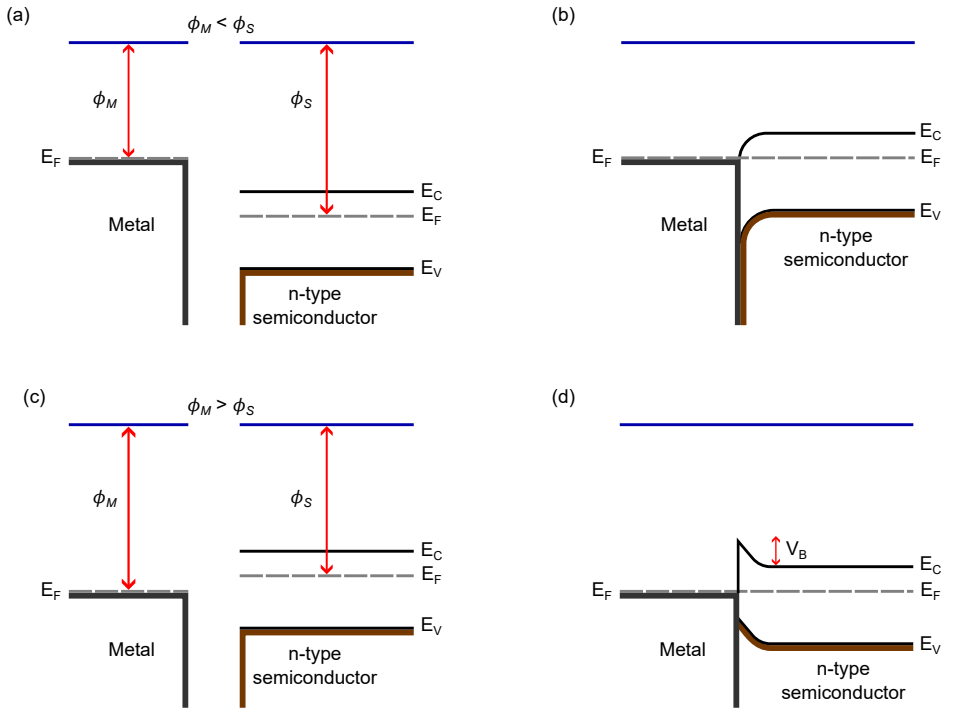

Figure 4. Formation of ohmic and Schottky contacts for n-type semiconductor. In (a) the metal work function ϕ_M is smaller than that of semiconductor ϕ_S, which leads to a formation of ohmic contact seen in (b). In (c) the metal work function is greater than that of semiconductor, leading to a Schottky type contact and the formation of potential barrier V_B seen in (d).

drain [52]. In a similar manner, the interfacial states increase the dark current in photosensitive devices, because the thermal excitation of charge carriers in the semiconductor increases via the defect levels, making the device less effective [53; 54]. With ohmic contacts, the density of states in the interface has been seen to directly affect the specific contact resistivity, and the low specific contact resistivity is not only a desired feature of ohmic contacts but also Schottky contacts [3; 55]. These problems highlight that further metal-semiconductor interface optimization is needed, especially since the meaning of interface increases as the device size decreases.

2.3.1 Device examples

Solar cells

The solar cell is a photovoltaic device that is used to generate electricity from sunlight. It is based on pn-junction between semiconductors and a photovoltaic effect. A schematic of a pn-junction with photovoltaic effect is presented in Figure 5.

As n- and p-type semiconductors are brought to a contact, they form a junction.

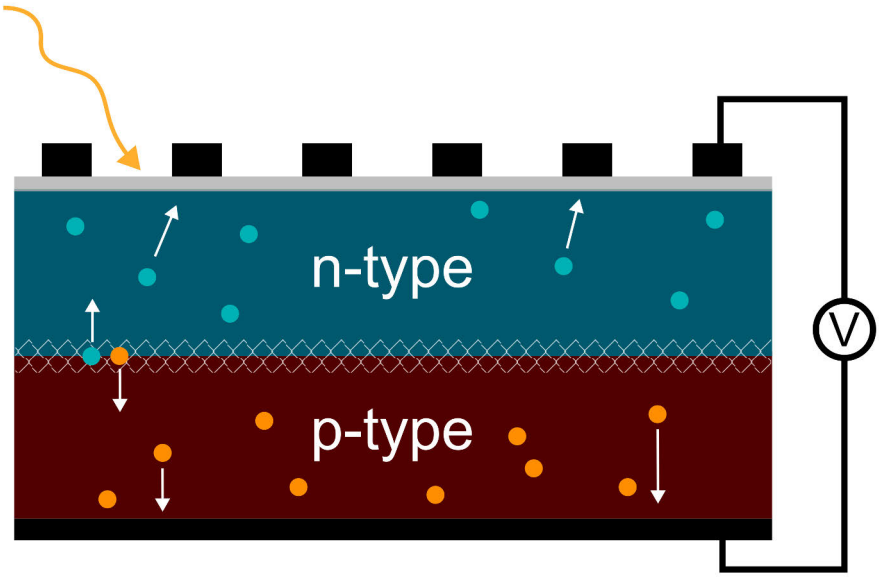

Figure 5. A schematic drawing of a solar cell. The p- and n-type materials form a pn-junction, creating a depletion region (white mesh). The electrons (blue dots) and holes (orange dots) generated by the photons (yellow arrow) drift to their respectful sides and to the metal contacts.

In the middle of the junction, a space charge region is generated. This creates an internal electric field, which moves the free electrons to the n-side and the holes to the p-side. As more and more carriers are packed to both sides, the carrier movement is slowed down. Eventually, the movement of charge carriers is halted as the junction is emptied from the free charge carriers. This empty space is called the depletion region, and if more charge carriers are generated, the internal electric field will separate them to their respectful sides. The pn-junction essentially turns into a Schottky diode once a metal contact is added [56].

The photovoltaic effect is essentially the electron excitation mechanism described in section 2.1.2 when the source of exciting energy is an incoming photon. In a solar cell, if the photon energy is sufficient and the p-n junction is excited, the generated electron in the conduction band and the hole left on the valence band will drift to opposite directions due to the internal electric field of the junction. This will create a voltage, which is effectively the output of the solar cell [57].

Metal-oxide-semiconductor field-effect transistor

One of the cornerstones of modern electrical devices is the metal-oxide-semiconductor transistor (MOSFET). It consists of a semiconductor substrate with certain doping, a source and drain regions with a semiconductor doped with high opposite doping, and a gate area in the middle with oxide layer. The substrate region between the source

and the drain, under the gate oxide, is called a channel. Essentially, the source and drain form a npn- or pnp-junction with the substrate, depending on the setup. A schematic figure of a MOSFET structure is presented in Figure 6.

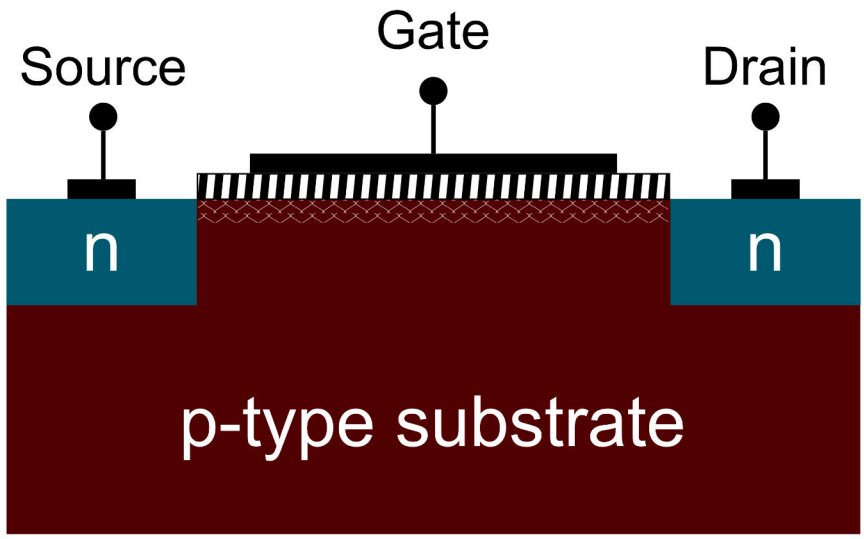

Figure 6. A schematic drawing of a MOSFET. Source and drain regions have opposite doping than the substrate, and a gate insulator is deposited between them (black and white striping). When voltage is applied to the metal contacts (black), a channel forms under the gate oxide (white mesh).

The source, drain and gate have metal contacts on top of them, and the gate is effectively a metal-oxide-semiconductor capacitor. When the voltage inserted into the gate is zero, there is no current flow between the source to the drain, meaning that the transistor is in off-state. This is due to a potential barrier generated between the source/drain and the channel area due to the opposite doping, blocking the flow of charge carriers. When the bias voltage is fed to the gate, the potential barrier starts to decrease. Once the bias voltage is greater than the threshold voltage, that is, the height of the potential barrier, the channel opens and the charge carriers can flow between the source and the drain. If the substrate is p-type, the source and the drain are n^{+}-type, and the current flow is from the source to the drain and the charge carriers are electrons. If the substrate is n-type, the source and the drain are p^{+}-type, and the current flows from the drain to the source as the holes act as charge carriers. [58]

3 Experimental methods

This chapter covers the experimental methods used in the research work of this thesis. Methods include ultra-high vacuum (UHV) surface science techniques combined with wet chemistry and electrical characterization. As a result of combining these methods, the materials and their properties have been thoroughly investigated, and changes as a result of treatments have been analyzed.

3.1 Ultra-high vacuum (UHV)

In order to avoid immediate reaction of the semiconductor surface with the environment after treatment/cleaning, a clean and a contaminant free environment must be established. This can be achieved using ultra-high vacuum. This is also the prerequisite for utilizing many surface science techniques since the particles used in the technique require a long mean free path so that they don't annihilate before they reach their target.

Ultra-high vacuum is defined as an environment having a pressure below 10^{-9} mbar, and a typical modern UHV system can easily reach pressures below 10^{-10} mbar. Such pressures are achieved using different types of pumping. The pumping configuration consists of roughing pump, which can be an oil rotary-vane pump or a dry scroll pump (also called a back pump in some context), a turbomolecular pump, and an ion pump. With roughing pumps, it is possible to achieve pressures of 10^{-3} mbar. To get lower than that, turbomolecular pumps must be used, which can enable low 10^{-9} mbar pressures. Ion pumps are required to get even lower than this. The roughing pumps and turbomolecular pumps are completely mechanical and base on either mechanical pressing of the gas molecules in cyclic manner or fast rotating blades which collide with gas molecules and direct them through the structure of rotating and stationary blades, respectively. Ion pumps, on the other hand, rely on high voltages giving stray electrons enough energy to ionize gas molecules in the event of collision, which are then collected in the ion pump by having the ions react with the Ti layer on the pump walls and stick there. Pumps also have the possibility for Ti sublimation to create a new covering layer to refresh the Ti coating on the pump walls. [59]

UHV requires tight sealing between the components, which can also withstand the great pressure difference. While welding the parts together is a solid method

to create air-tight connection, it denies modification and modularity of the UHV system, which is why only the actual UHV chamber is assembled by welding. As for flanges, ports and view ports knife-edge or ConFlat flanges is used. Usually made from stainless steel as the chamber itself, two flanges are sealed together by placing a soft metal gasket between the flanges and tightened together with bolts. The knife edges in the flanges penetrate the soft metal gasket, creating the seal. Copper is the most used and reliable gasket material, but nickel and aluminum are also possible materials. The bolts used to join the flanges have to be the same material as the flanges so that the whole joint expands uniformly in elevated temperatures. [60]

For pressure measurement, three main gauge types are used: Pirani, cold cathode, and hot cathode. The Pirani gauge is based on a wire heated with current, and the wire is part of a Wheatstone bridge circuit. A change in the pressure leads to a change in the thermal conductivity, which changes the temperature of the wire, which ultimately leads to a change in the resistance of the wire. The change in the resistance can be used to monitor the pressure. The most sensitive and accurate way to operate the setup is to keep the resistance of the wire constant by varying the voltage fed to the bridge. Pirani gauges can measure pressures down to 10^{-3} mbar [61]. For lower pressures, cold or hot cathode gauges are needed. In the cold cathode gauge, a DC voltage in the kilovolt range is used to create a gas discharge between the anode and the cathode. The discharge generates electrons, and with the magnetic field, the path of the electrons is increased by forcing the electrons to travel in spirals. The spiral trajectory increases in the path length compared to a direct anode-cathode path, thus generating more ionizing collisions resulting in a broader measurement range. The current generated by the ions that reach the cathode is used to determine the pressure. A reasonable measurement range for such a gauge is between 10^{-2} mbar and 10^{-8} mbar [62]. The hot cathode gauge uses a glowing cathode to generate electrons. The generated electrons are accelerated to the anode, where they collide with gas molecules, which ionize and when reaching the ion collector generate the ion current, which is used to determine the pressure. In the most common type of hot cathode gauges, Bayard-Alpert ionization gauge, the electrons generated by cathode wires are accelerated to the cylindrical mesh anode, where they ionize the gas molecules. The collector is a thin wire in the middle of the anode on the axis of the cylindrical mesh. The reason for the construction is to minimize the effect of soft x-rays, which form when the electrons collide with the anode. When the x-rays hit the collector, the photoelectrons are released, and the current loss from this would give a falsely high pressure reading. The measurement limit for Beyard-Alpert gauges can be as low as 10^{-13} mbar [61; 62].

The UHV system used in this work consisted of three chambers: load lock, preparation chamber, and analysis chamber separated by gate valves. Samples of 6 x 12 mm^2 were introduced into the system via the load lock pumped with turbo pump. The load lock was connected to the preparation chamber pumped with turbo

and ion pumps. The preparation chamber consisted of a sample manipulator with a resistive heating element, a selection of different evaporators (not used in this work), and a needle valve for introducing gasses into the chamber. The base pressure in the chamber was 1×10^{-8} mbar. The preparation chamber was connected to the analysis chamber, which was also pumped with turbo and ion pumps. The analysis chamber featured a sample manipulator with resistive heating element and a direct current heating setup, x-ray photoelectron spectroscopy (XPS), scanning tunneling microscopy/spectroscopy (STM/STS), and low-energy electron diffraction (LEED) instrumentation. The base pressure in the analysis chamber was 5×10^{-10} mbar. The schematic structure of the used system is presented in Figure 7.

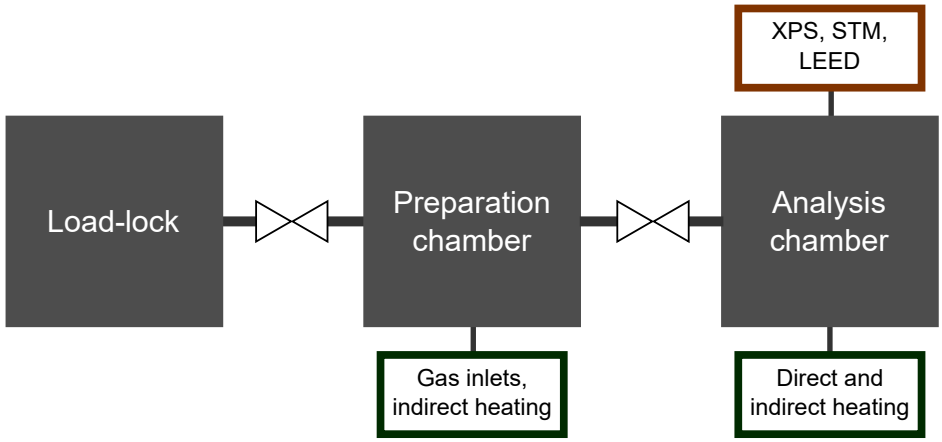

Figure 7. A schematic drawing of the used ultra-high vacuum system.

3.2 Preparing the semiconductor surface

In order to understand how the semiconductor surface and the deposited metal interact, the surface prior to metal deposition has to be optimized. The principal methods used here are wet chemistry and UHV treatments.

3.2.1 Wet chemistry

Wet chemistry was used for two purposes: cleaning/treating the surface and removing metal from the surface after lithography.

For silicon surface cleaning, the full Radio Corporation of America (RCA) procedure with HF dip, and only HF dip was used. RCA utilizes sulfur acid (H_2SO_4), hydrogen peroxide (H_2O_2), ammonium hydroxide (NH_4OH), hydrochloric acid (HCl) and de-ionized water (DIW), and the procedure was as follows: 3 minute ultrasonic baths in acetone, methanol, and 2-propanol followed by N_2 drying. Following ul-

trasonication, the sample was immersed in a $80\,^{\circ}\mathrm{C}$ Piranha solution consisting of H_2SO_4 (95-97 %):H_2O_2 (30 %) (3:1). After this, the sample was inserted into the $80\,^{\circ}\mathrm{C}$ SC-1 solution of NH_4OH (28-30 %):H_2O_2 (30 %):DIW (1:1:5) followed by an immersion into a $80\,^{\circ}\mathrm{C}$ SC-2 solution of HCl (37 %):H_2O_2 (30 %):DIW (1:1:6). The final step was to immerse the sample into a 5 % HF solution for 5 seconds to remove the silicon oxide from the surface and passivate the surface by hydrogen termination to prevent native oxide from forming in air. After each step except the ultrasonications, the sample was rinsed with DIW and blow dried with N_2. The other treatment was to immerse the sample in a 5 % HF solution for 5 seconds followed by DIW rinse and N_2. The GaN surface was treated for 1 minute in $60\,^{\circ}\mathrm{C}$ 4 M potassium hydroxide (KOH) solution followed by immersion in DIW for 1 minute.

3.2.2 UHV treatments

Two main UHV treatments for semiconductor surfaces were used: heating and gas exposure. Both treatments were possible at the same time in the UHV system introduced in 3.1. The UHV system provided a possibility to heat the semiconductor samples by either conducting current straight through the sample (later referred to as direct heating) or by using a heater in the sample manipulator beneath the sample (later referred to as indirect heating). Direct heating was used for silicon to achieve temperatures as high as $1250\,^{\circ}\mathrm{C}$ fast (later referred to as flash heating). To prevent excessive pressure increase due to the outgassing of the sample, the treated sample was initially degassed in $600\,^{\circ}\mathrm{C}$ for multiple hours to allow the vacuum recover from pressure increase resulting from heating the sample to the degassing temperature. The purpose of degassing was also to remove carbon contamination, which can cause a formation of unwanted SiC clusters at elevated temperatures. One cycle of flash heating was done by quickly ramping the temperature to $1250\,^{\circ}\mathrm{C}$, keeping the temperature for 5 seconds and returning to $600\,^{\circ}\mathrm{C}$. This was repeated 5-10 times.

Indirect heating consisted of tungsten wire bend so that it formed an rectangular heater. Wire was covered with ceramic insulator to prevent short-circuiting. Element was located in the manipulator in a position where the sample holder was placed so that the element was directly under the sample holder. Indirect heating was used to heat the samples up to $500\,^{\circ}\mathrm{C}$, and in opposite to the flash heating cycle, the heating time was up to 1 hour. Both direct and indirect heating's were conducted in the analysis chamber.

For gas exposures, a leak valve connected to the preparation chamber was used. Gas was selected by adjusting the valves at the valve table connected to the gas bottles including O_2, H_2 and NH_3. Gas was introduced to the chamber by slowly opening the leak valve and observing the pressure. Typical gas exposure was done at 5×10^{-6} mbar partial pressure while pumping with a turbo pump. In case of combining heating and gas exposure, the temperature was first set to the desired

value and then the leak valve was opened to achieved the desired partial pressure.

3.3 Surface characterization techniques

Three different ultra-high vacuum surface characterization methods and one contact resistivity measurement method were utilized in this work. X-ray photoelectron spectroscopy was used for characterizing the chemical composition of the surface, low-energy electron diffraction was used to determine the surface structure and reconstructions, and scanning tunneling microscopy/spectroscopy to scan the surface topology on the atomic level as well as measuring local density of states to determine the band gap of the surface.

3.3.1 X-ray photoelectron spectroscopy

X-ray photoelectron spectroscopy is used to characterize the chemical composition of the upmost surface. It is based on the photoelectric effect. As the material absorbs a photon, the photon gives all its energy to the material system of which energy states change via the electron-level occupation. If the energy of the photon is greater than the binding energy of the electron in the solid material, i.e., the energy required to remove the electron from the material to the vacuum, the electron is removed from the material and a photoelectron is created. The kinetic energy of the photoelectron in this case is

$$E_k = h\nu - E_b - \phi, \tag{5}$$

where $h\nu$ is the photon energy, E_b is the binding energy of the electron and ϕ is the work function of the spectrometer. The work function can be defined by measuring the spectrum of a known material, e.g., gold, and adjusting the work function so that the measured spectrum matches the reference spectrum. Since the energy of the incoming photon can vary according to used x-ray source, it is more convenient to use electron binding energy in the analysis, which can be presented as

$$E_b = h\nu - E_k - \phi. \tag{6}$$

Common x-ray radiation sources in commercial devices are Al k-α and Mg k-α x-ray tubes with photon energies of 1486.6 eV and 1253.6 eV, respectively. X-rays can also be produced by using a synchrotron, for which a separate facility has to be built (please see the subsubsection "Synchrotron radiation x-ray photoelectron spectroscopy"). [63]

To achieve discrete spectra, the incoming radiation has to be monochromatic, and in case of Al the system needs to have an additional monochromator. In addition to the x-ray source the measurement equipment consists of analyzer for distinguishing

the photoelectrons and a detector to receive the information about the photoelectron energies. As the photoelectrons are removed from the material, they fly to the analyzer. Extraction optics at the beginning of the analyzer gather the electrons so that the electrons can enter the analyzer only with a certain trajectory. The kinetic energy required to enter the analyzer can also be regulated by adjusting the pass energy. Higher pass energy enables larger amount of photoelectrons to enter the analyzer with a cost of resolution and vice versa. After the extraction optics the photoelectrons enter the hemispherical analyzer. The hemispherical analyzer consists of two hemispheres with a voltage difference between them. This voltage modifies the trajectory of the photoelectrons according to their entering kinetic energy, so that once the photoelectrons reach the detector, they hit different spots on the detector which makes the determination of different energies possible [63; 64; 65]. A simple schematic of an XPS setup is shown in Figure 8.

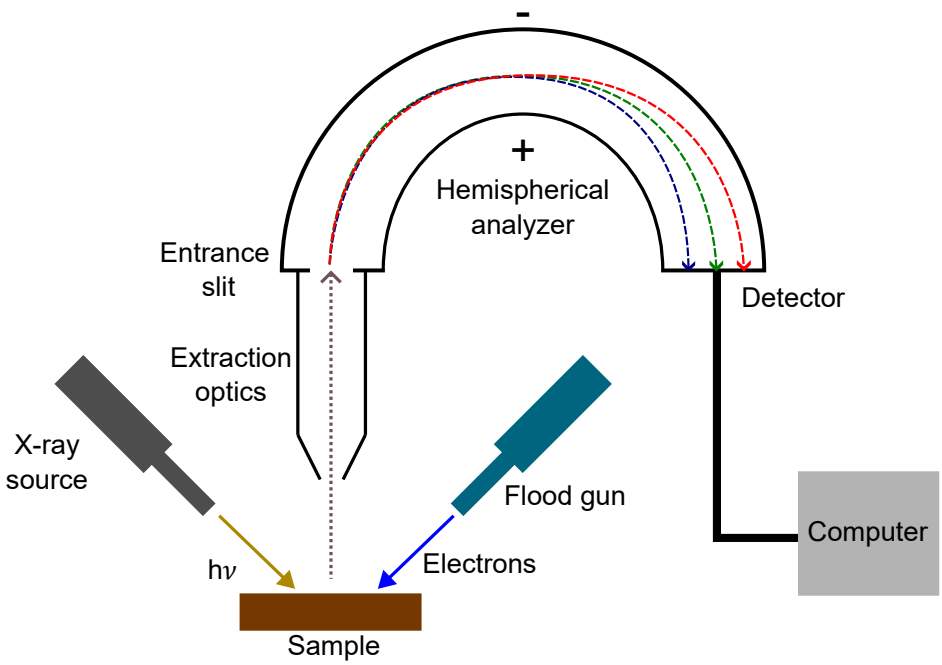

Figure 8. A schematic drawing of an XPS measurement setup.

The penetration depth of the x-rays is dozens of micrometers, however due to collisions between other particles the escape depth of the photoelectrons is roughly less than 10 nm depending on the material. The intensity of the received signal depends on the electron core where the photoelectron escapes: deeper the core level is, the higher the measured binding energy is. In addition to this, the physical escape depth of the photoelectron affects the signal intensity, enabling depth analysis without a need for depth profiling using sputtering: by measuring photoelectrons from

deep core levels known to have low intensity, low kinetic energy and small escape depth, it's possible to distinguish if the measured material is right at the surface or deeper. [66]

If the material is insulating, the loss of photoelectrons can lead to positive charging of the surface. This will cause a shift in the measured core-level spectrum towards higher binding energy due to opposite charges if the surface and the photoelectron, and cause broadening in the peaks. Shift in core-level spectrum makes the chemical composition analysis difficult as the binding energy of the electrons depends on the bonding environment of the atoms in the material. In turn the broadening of the peaks causes the component crystallinity analysis difficult, as the sharpness of the peaks is directly proportional to the crystallinity of the measured material component. This can be compensated with a separate electron gun, which shoots electrons to the surface. The electron flux from the electron gun has to be adjusted to match the electron loss of the surface. [63]

Two XPS devices were utilized: one with non-monochromatized Mg k-α with spot size of 3-4 mm in the UHV system (in-situ XPS), and Thermo Scientific Nexsa system with monochromatized Al k-α with charge compensation and adjustable spot size (ex-situ XPS). In-situ XPS was used to characterize the surface during UHV processing, while ex-situ XPS was used to determine surface composition after metal deposition and study the effect of air exposure to the treated surfaces.

Synchrotron radiation X-ray photoelectron spectroscopy

For more accurate photoelectron spectroscopy, a synchrotron radiation source is needed. Compared to standard laboratory XPS like described earlier, synchrotron radiation x-ray photoelectron spectroscopy (SR-XPS) require facilities that are much more complicated. Figure 9 shows the basic structure of the synchrotron radiation facility. [67] An electron gun produces electrons that are guided through a linear accelerator (linac). Once the electrons are accelerated, they move to the booster ring. Here the electrons are accelerated further, typically to the energy of the electrons which are in the main storage ring. The electrons from the booster ring are fed to the storage ring but only when the current in the storage ring drops to a certain threshold. The storage ring holds the electrons used to produce the synchrotron radiation. The electrons in storage ring have energies of GeV's, and are traveling close to the velocity of light. [67]

Despite the name "ring", the storage ring isn't a perfect circle but has corners and straight lines. Ring-like form is made with bending magnets at the corners, which deflect the electrons so that they change their trajectory along the ring. Change in the trajectory generates radiation, but the insertion devices at the straight parts are the main source of the radiation. Insertions devices alter the trajectory of the electrons back and forth, and the change in the travel direction results radiation. Either wig-

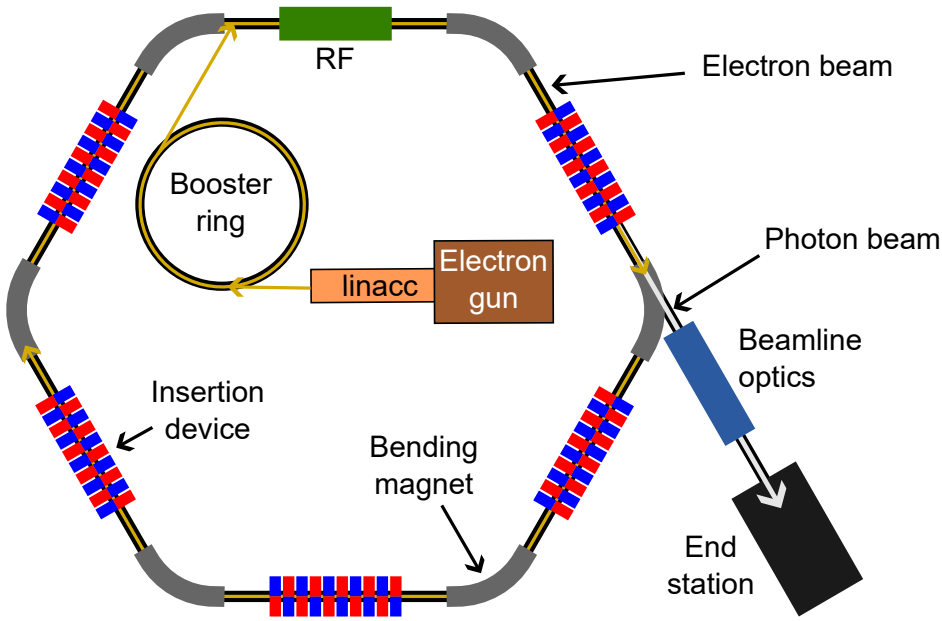

Figure 9. A schematic drawing of a synchrotron radiation facility. Only one beamline is drawn here as an example, but in reality after every insertion device there is a beamline.

glers or undulators can be used as insertion devices, and they have similar working principle of consecutive opposite magnets causing back and forth movement in electron path, except that the magnitude of the movement is different with the two. With undulator the movement is smaller, resulting in narrower radiation beam. Emission of the synchrotron radiation causes losses in electron energy, which is compensated by radio frequency (RF) supply. The energy of the electron is raised back to the storage ring energy every time the electron passes through the supply. [67]

Beamline is placed along the straight parts of the ring, tangentially to the bending magnets. After the front end of the beam, which separated the storage ring from the beamline, the optics modify the beam and are customary to each beamline depending the purpose of the beamline. The final stage is the end station or the experimental hutch, in where the actual experiment is performed. [67]

One of the greatest benefits of synchrotron radiation in surface surface composition analysis is the tunability of photon energy. Even with small photon energies the attenuation length of the photon is easily hundreds of nanometers, meaning that the photons penetrate much deeper than the surface layer usually is. However, the photoelectron attenuation length is significantly smaller, in the range of nanometers. By adjusting the photon energy, the attenuation length of the photoelectron, i.e., the signal depth, can be adjusted. This enables measuring the surface composition at different depths, even below 1 nm, in comparison to XPS equipment with a fixed energy photon source [68].

The experiments were conducted in the MAX IV synchrotron facility at the 1.5 GeV storage ring at the FinEstBeAMS beamline. Unlike in Figure 9, MAX IV doesn't use booster ring but accelerates electron only using linear accelerator. The beamline consists of two branch lines and three end stations, of which the solid state end station (SSES) was used [69; 70]. The source uses undulator type insertion devices, and the beam goes through baffles, mirrors and plane grating. Beam is divided to branches with exit slits, which are followed with higher-order suppressing filters before mirror directing the beam to the end station.

3.3.2 Low-energy electron diffraction

Low-energy electron diffraction is a surface crystalline structure characterization method which utilizes electrons with energies ranging between 20-500 eV directed to the sample surface. Incoming electrons have a wavelength λ, which is reciprocally connected to the wavevector k. The magnitude of this wavevector can be used as a radius of the Ewald sphere, which illustrates the diffraction condition. In three dimension presentation Ewald sphere covers a region consisting of lattice points. To simplify, presenting it in two dimensions enables presenting the diffraction condition using rods rather than points [65]. Figure 10 demonstrates the use of Ewald sphere. As the electron beam hits the surface, the electrons interact with the first less than

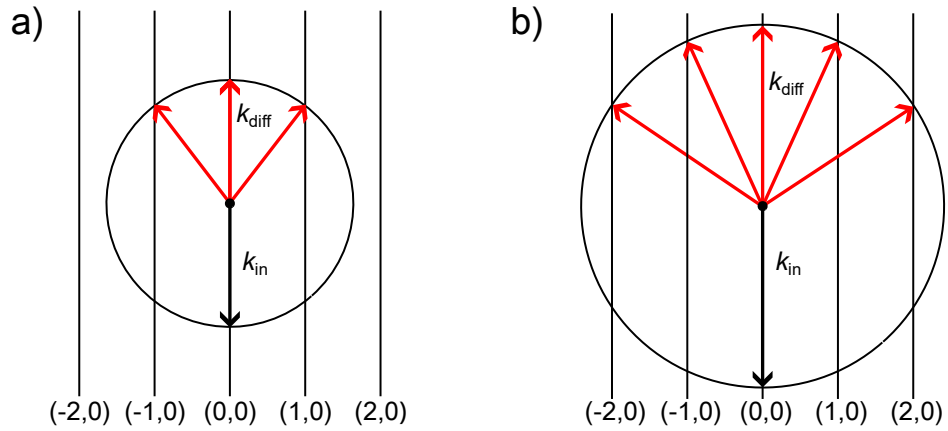

Figure 10. The principle of the Ewald sphere with a) lower and b) higher electron energy. The radius of the sphere is determined by the magnitude of the incoming electrons wavevector k_{in} and thus its energy; higher the energy, larger the sphere. The diffraction condition is satisfied when the elastically scattered wavevector k_{diff} has a direction towards the intercept of Ewald sphere and the rod.

10 atom layers and both elastically and in-elastically scattered electrons are created. Elastically scattered electrons have the same energy as the incoming electrons, and thus their wavevector magnitude is also the same. This is also why the surface sensitivity of LEED is much higher than that of XPS, because the elastic electrons first

have to travel to the material and then back to the vacuum. Every elastically scattered electron wavevector that is directed to the intersection of Ewald sphere and the rod satisfies the diffraction condition and creates a spot in LEED pattern. As a result of the conservation of momentum, diffraction can only occur within the range of the Ewald sphere. Two dimensional LEED spots are annotated using Miller indices h and k. Increasing the energy of the incoming electrons creates a larger Ewald sphere, which leads to increased amount of spots visible in LEED. [65]

The experimental setup consists of electron gun, a set of grids with varying electrical potentials and a fluorescent screen, and is presented in Figure 11. The electron gun is directed to the sample surface and is used to produce the incoming electrons. As the electrons hit the surface, both elastically and in-elastically scattered electrons are generated. The majority, 95-98 % of the scattered electrons are in-elastically scattered. Once the electrons scatter from the surface, they travel towards the fluorescent screen through a set of three grids with varying electrical potentials. Small negative potential between grid 1 and grid 2 filters most of the in-elastically scattered electrons out but lets the elastically scattered electrons pass. Grid 3 and the fluorescent screen has large potential difference, which is used to accelerate the electrons towards the fluorescent screen. Filtering the in-elastically scattered electrons out helps to reduce the bright background in the fluorescent screen and accelerating the scattered electrons ensures that they can excite the fluorescent material in the screen to show the diffraction pattern. [71]

3.3.3 Scanning tunneling microscopy/spectroscopy

Scanning tunneling microscopy is a measurement technique that provides the possibility to determine the topography of the surface at the atomic level. It utilizes tunneling current I_t between the sample and a sharp tip which is linearly dependent on the local density of states at the surface. Tunneling current is also exponentially proportional to the root of the potential barrier ϕ and distance between the sample and the tip d as follows:

$$I \propto e^{\sqrt{\phi}d}. \tag{7}$$

Due to the exponential proportionality of current to the distance, even a slight change in the distance causes significant change in the current and vice versa, the tip has to be very close to the surface in order for tunneling to occur [72; 73]. Due to this the tip also has to be very sharp, ideally atomically sharp, since the tunneling current will flow from any atomic-scale feature on the tip when brought close to the surface. If the radius of the tip is large, tunneling can occur from multiple spots on the tip, leading to poor resolution. In reality, getting a atomic sharpness is not possible but the radius of a realistic atomic resolution tip is a few hundred Å [74; 75].

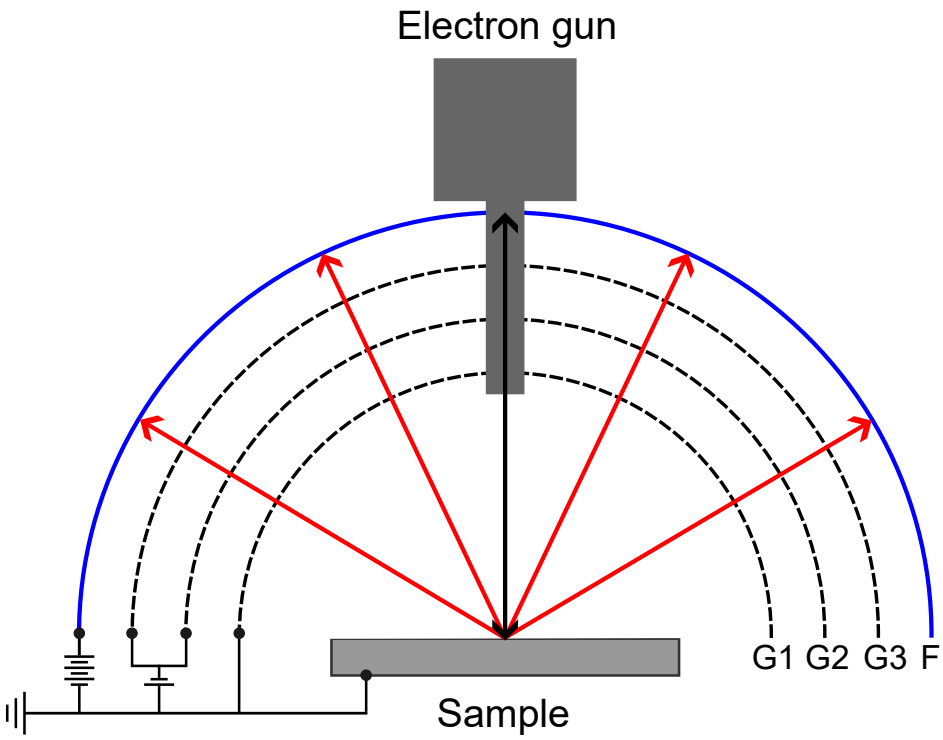

Figure 11. A schematic of the LEED measurement equipment. Grids 1, 2 and 3 are labeled as G1, G2 and G3, respectively, and the fluorescent screen as F.

Although the measured topography figure can be considered to represent the real-space structure of the surface, i.e., atom structure and order on the surface, in reality STM gives information on the electronic structure of the surface. In the resulted image the dots representing the atom locations are in fact electronic states. Electronic states follow the same symmetry than the actual atoms on a local scale, but it is not possible to determine the exact location of the surface atoms with single STM measurement. However, local symmetry is sufficient to determine atomic steps and flat terraces. [76]

A simple STM measurement equipment is shown in Figure 12. A basic measurement setup consists of a sample, a sharp metal tip usually made of W, piezoelectric drives for tip or sample manipulation, vibration isolation, a feedback loop, and a control unit. Depending on the setup, either the tip or the sample is connected to xyz piezodrives. Using the z piezo, the sample and the tip are brought closer to each other. The user can make a coarse approach, but the final approach to the measurement distance is done by the control unit. With preset gap voltage V_{g} and current values, the control unit moves the sample and the tip closer to each other step by step while monitoring the tunneling current with the feedback loop. Once the preset value for tunneling current is achieved, the approaching is stopped and the setup is ready

for measuring. A sawtooth voltage is applied to the x piezo and a ramping voltage is applied to the y piezo, which results in a xy plane imaging. The voltage between the sample and the tip can be either positive or negative: with a positive voltage the electrons tunnel from the occupied states in the tip to the empty states in the sample, and with a negative voltage the tunneling occurs from the occupied states of the sample to the empty states in the tip. Since the distance between the sample and the tip is only a mere fraction of a nanometer, even a small vibration can prevent one from obtaining an atomic resolution image. Hence, the vibration isolation is crucial and the disturbance has to be less than a picometer. The damping system based on suspension springs with eddy-current damping is considered to be one of the most efficient one. [73; 75]

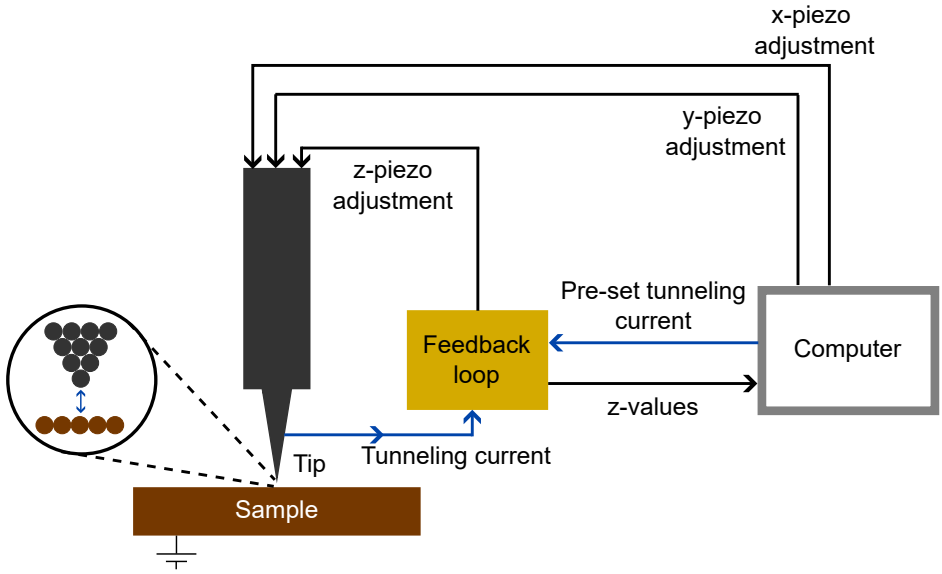

Figure 12. A schematic of the STM measurement equipment.

For topography measurement, a constant current mode is used. Since the current is proportional to the current between the sample and the tip, while scanning the surface with constant current, the distance should remain approximately the same. During xy scan, should the surface have, for example a terrace step, as the tip goes over the step, the tip height is adjusted so that the current remains constant. By tracking the z piezo voltage, the variation in the height of the tip can be monitored, and from this the topography of the sample surface can be constructed for the image. It is also possible to use the constant height mode so that the height of the tip stays the same and the changes in current are observed. Having a constant tip height requires slower feedback and a very smooth sample surface so that the tip does not hit a higher feature on the surface. The information gathered from either the constant current mode and the constant height modes is generally close to each other, and since the

constant current mode is more safe from the point of view of tip preservation, it is used more. [74]

In addition to topography measurement, STM equipment can be used for scanning tunneling spectroscopy. In contrast to STM which gathers information about the surface by rastering, the STS measurement is based on keeping the tip at a certain point on the surface and measuring the local density of states with varying gap voltage. Typically, the point is selected from the STM image so that the surface condition is known before the STS measurement, but it is not mandatory. Varying the gap voltage results in an I-V curve, from which a figure of a dI/dV_{g} as a function of the gap voltage V_{g} can be drawn. This figure can be used to analyze the band structure on the surface: at 0 V is the Fermi energy, and generally the voltage area with dI/dV_{g} equal to 0 around the Fermi energy is considered to mark the band gap.

For measurements presented in this thesis, the Omicron Scala STM/STS was used. All measurements were performed at room temperature.

3.4 Specific contact resistivity measurements

For determining specific contact resistivity ρ_c a transfer length method (TLM) was used. The method utilizes a set of metal contacts with length L and width W placed on the semiconductor surface with increasing distance d_n as seen in Figure 13. By measuring voltage drop between the contacts with increasing contact spacing it is possible to determine contact the resistance without knowing the sheet resistance of the material layer below the contacts. Based on the IV curve measured between the

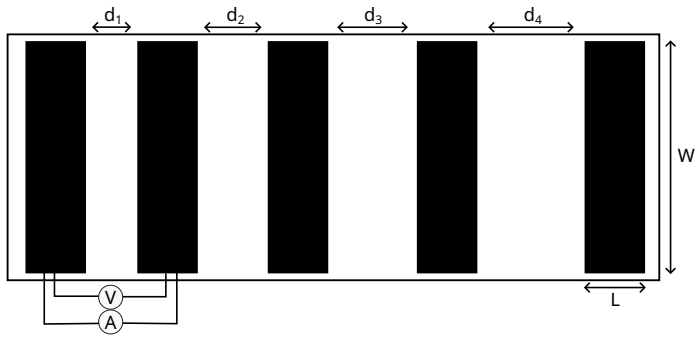

Figure 13. TLM structure.

metal contacts it is possible to calculate the total resistance R_T between the contacts. Plotting the resistance values as a function of contact distances gives a slope, which can be used to determine the contact resistance R_c. Figure 14 shows that the contact resistance is half of the intercept value of the y-axis. This value could be used to calculate the contact resistivity since the contact dimensions are known, however the current doesn't flow through to the whole contact but only through the edge of

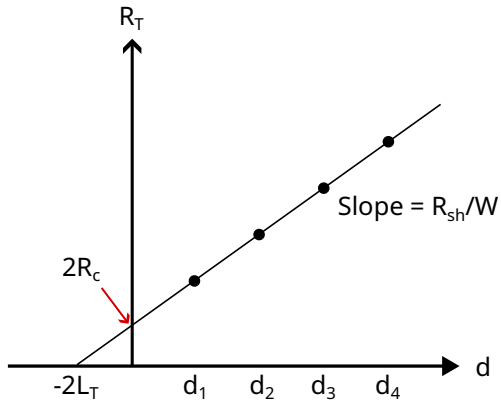

Figure 14. As a result of TLM measurement a plot between total resistance and the contact distance can be formed. The contact resistivity R_c and the effective contact length L_T can be determined using the slope from the plot.

the contact. This effect called current crowding has to be taken into account, and the effective contact length L_T can be determined as a negative half value of the intercept of the x-axis. [48]

Thus, the specific contact resistivity is calculated using the following equation:

$$\rho_c = R_c W L_T. \tag{8}$$

The contact resisitivity measurements were conducted using Rucker & Kolls 666 probing stage connected to the HP4145B semiconductor parameter analyzer, which was controlled with a LabView program.

3.4.1 Sputter deposition

The most basic sputtering setup consists of a vacuum chamber, a gas inlet, a metal target working as cathode, a sample plate working as anode and a power source. Once a sufficiently large voltage is applied between the anode and the cathode, the argon gas fed into the vacuum chamber at low vacuum range forms a plasma discharge. The metal target working as cathode draws the positively charged argon ions towards itself. As the ions hit the metal target, metal atoms are detached from the target and fly to the anode where the metal is wanted to be deposited. [77]

Metal layers for TLM measurements were deposited using Bal-tec MED-020 sputtering device. The metals used were platinum and nickel, and the metal layer thicknesses ranged from 3 nm to 270 nm.

3.4.2 Contact patterning

For contact patterining, two different lithography methods were used; ”standard” and lift-off. In standard lithography, a metal layer covering the whole surface was deposited on the sample after the surface treatments. After this, the surface was cleaned with acetone and IPA before spreading the positive photoresist on the surface by spinning. After spinning, the photoresist was baked at $115\,^{\circ}\mathrm{C}$ for 1.5 minutes on a hot plate. This so-called softbake was done to decrease the amount of solvent in the deposited resist, thus improving resist adhesion to the surface and decreasing the risk of mask contamination and mask sticking to the resist. After baking, a shadow mask with the contact pattern was placed on top of the sample and the surface was radiated with UV light for 80 seconds. The photoresist exposed to UV radiation was dissolved in 0.15 M NaOh solution acting as a developer. As a result, the surface had photoresist only at the spots where the contacts were wanted to be formed. Since the surface still had excess metal around the desired contact areas, the metal had to be etched away. For Pt, the etching solution was boiling aqua regia consisting of HCl (37 %):nitric acid (HNO_3) (65 %) (1:1), and for Ni the solution was room temperature HCl (37 %):DIW (1:2). With both solutions, the etching time was determined based on the visible changes on the surface. The remaining photoresist on top of the contacts was removed with acetone, followed by IPA rinse and drying with N_2.

In lift-off lithography, photoresist deposition and patterning was done before the metal deposition. In this case, the desired contact pattern was patterned to the photoresist so that the resist layer had holes on the spots where the final metal contact was meant to be. The photoresist was patterned using the Kloé Dilase 250 laser writer. At this stage, it was still possible to do surface treatments which did not interfere with the photoresist layer, such as HF dipping. After the surface was patterned, a metal layer was deposited on the surface. The excess metal was removed by removing the photoresist beneath it using acetone, followed by IPA rinse and drying with N_2.

The contact pattern used for the TLM measurements consisted of four rows of rectangular contacts with dimensions of $300\,\mu\mathrm{m}$ x $600\,\mu\mathrm{m}$. The distance between the first two contact columns was $300\,\mu\mathrm{m}$, and the distance increased by $100\,\mu\mathrm{m}$ after each column. From each sample, at least four contact pairs were measured from at least two contact rows to get a sufficient amount of data for plotting and analysis.

4 Summary of publications

4.1 Effects of Ultra-High Vacuum Treatments on n-Si Contact Resistivity

We investigated the effects of combining wet chemical and UHV treatments on n-type Si contact resistivity. The motivation for this research topic was to see how the surface of (100) silicon could be improved from the contact resistivity point of view, because UHV has not been used much in metal contact manufacturing. The impact of the treatments was tested with low and highly phosphorus doped n-type silicon. Wet chemical treatments included Radio Corporation of America (RCA) cleaning with HF dip in the end, and a stand-alone HF. UHV treatments consisted of annealing's ranging from $400\,^{\circ}\mathrm{C}$ to $1200\,^{\circ}\mathrm{C}$. Surface properties were defined using XPS, LEED and STM, and contact resistivity was measured using TLM.

For low doped n-Si the best treatment was a combination of $1200\,^{\circ}\mathrm{C}$ heating ("flash heating") followed by 5 s HF dip. The surface after the flash heating was smooth with 2D terraces with visible dimer rows in STM and (2x1)(1x2) reconstruction in LEED. Surface was cleaned from oxygen and carbon contaminants, and the oxide formation during transfer from UHV to HF dip was small. Passivation provided by the HF dip proved to hold well, and before metallization only very minor sub-oxide formation was seen. For highly doped n-Si this, however, was not as successful treatment. In fact, the contact resistivities measured from both low and high doped samples were the same.

The main issue with flash heating for high doped n-Si was dopant out-diffusion. Such high temperature caused doping atoms to diffuse out from the surface, decreasing the doping concentration and thus increasing the contact resistivity compared to just HF treated sample. This was also visible in STS curves, where the surface seemed to change from n-type to p-type due to band bending occurring from doping concentration difference between the very surface and the area beneath it. Decreasing the temperature to $400\,^{\circ}\mathrm{C}$ helped to keep the dopant atoms on the surface, thus decreasing the contact resistivity when combined with HF treatments.

The doping concentration played a crucial role in the current flow mechanisms in the samples, as the contact resistivity measured from low doped n-Si turned out to origin from a silicide alloy at the interface rather than from an actual ohmic contact. The alloy formation was conclude to occur already during metal deposition phase

without any annealing, causing the current to flow through the silicon-metal channel. Alloying was clearly visible in measured XPS spectra from between the metal contacts. Surprisingly, the resistivity of the alloy reacted to the surface treatments, indicating that the silicon surface structure affects also the silicide properties. When replicating the experiments with low doped silicon but using lift-off lithography, the measured contacts were Schottky type. With high doped silicon the measured contact resistivities were the same with both standard and lift-off lithography, indicating that the values obtained from high doped silicon were actual contact resistivities, and the current flows beneath the silicide layer in the semiconductor.

Experiments showed that the selection of a correct lithography method is crucial in contact manufacturing. It is not only a matter of convenience, i.e., no need to select a metal specific etching solution with lift-off, but also an important aspect in achieve realistic contact behavior. But, despite the alloy formation, the electric properties of the alloy was dependent on the surface treatment of the silicon. Also, a high enough doping concentration enabled current flow past the alloy and straight through the semiconductor.

4.2 Surface Properties of p-GaN and Formation of Nickel Metal Contacts

Low-resistivity ohmic metal contacts have proven to be difficult to manufacture on Mg doped p-type gallium nitride. Difficulties in doping activation, high Schottky barrier and Mg-H complexes mean that just increasing the doping concentration doesn't yield low contact resistivity. Annealed stack of Ni and Au has provided low contact resistivity contacts due to Ga solubility to Au, but they can not be used if p-GaN CMOS technology is to be integrated to Si CMOS processing lines. We investigated a simple system of Ni metal contacts on p-GaN to investigate, whether it is possible to fabricate ohmic contacts with only Ni and if yes, what happens at the interface. Prior to metal contact experiments, the surface of the p-GaN was investigated to understand the starting surface. Surface was investigated using XPS, LEED and STM. Electrical measurements were done using TLM and the metal-semiconductor interface was characterized using SR-XPS.

Prior to any treatments, the p-GaN surface showed a clear hexagonal (1x1) LEED pattern and large terraces in STM. Closer imaging in STM showed that the surface has flat areas with white dots. After the KOH treatment the LEED pattern got brighter and the white spots disappeared from STM close-up. KOH clearly removed something from the surface, and XPS measurements showed a change in Mg 1s spectra towards more metallic line shape. As there were no changes in Ga 3d spectra but the amount oxygen reduced, we concluded that the change in Mg 1s and thus also in STM close-up is a result of KOH removing MgO from the surface. However, the surface most likely still had gallium oxide, as no change was observed in Ga 3d and

surface still clearly had oxygen.

Annealing was crucial to obtain ohmic contacts; without any annealing, the contacts were Schottky type. The resistivity and the result uniformity depended on the annealing background: by annealing only in UHV, the resistivity wasn't uniform when measured from different contact rows. By annealing in NH_3 background gas at 5×10^{-5} mbar partial pressure the resistivity did not only half, it also was significantly more uniform. Benefit of NH_3 background gas was suggested to be the suppression of nitrogen vacancies which can work as a compensating n-type doping.

SR-XPS measurements showed that as a result of UHV annealing an additional Ga component is created. The sample annealed with NiO on the surface had a clear Ga peak with 500 eV photons, and inspection with very surface sensitive 200 eV photons showed two sharp Ga peaks. Diffusion of Ga to the surface was clear since no Ga was observed even with high energy photons prior to the annealing. Sharp additional Ga component was also observed in the sample with NiO removed before annealing. Since the spectra measured from this sample also had signal from Ga-N region due to thinner capping layer, the binding energies of KOH treated and metal capped UHV annealed surfaces could be compared; the UHV annealed surface showed a clear shift in Ga 3d spectra towards higher binding energy.

Combination of contact type change and the changes in XPS lead to a conclusion that the diffusion of gallium to the nickel layer left gallium vacancies to the interface. These vacancies generate extra electron levels which lie in the band gap close to the valence band and act as a path for the charge carriers to tunnel through the Schottky barrier. Annealing also caused nitrogen diffusion, which could be suppressed using NH_3 background gas, but the effects to the chemical composition of the interface should be investigated more to determine the role of the background gas more accurately.

4.3 Potential of ultrahigh-vacuum based surface treatments on silicon technology

Despite UHV being clean and controlled environment for silicon processing, it is not that common in silicon technology. One of the issues is the high temperature which is considered to be needed to increase the crystallinity of the silicon surface. To investigate possibilities of making UHV more compatible with the industry, we conducted four different investigations: low temperature annealing of RCA cleaned and HF dipped Si in hydrogen partial pressure, UHV oxidation and annealing of flashed Si, post-annealing of RCA cleaned Si and oxidation of sidewalls of a commercial Si diode.

Annealing a RCA treated Si in H_2 background at $200\,^{\circ}\mathrm{C}$ increased the surface crystallinity; the surface sensitive LEED measurement with lower electron energies showed a clear increase in diffraction spot brightness. At the same time the carbon

concentration at the surface reduced by 2.5 times. The result shows that generation of atomic hydrogen or hydrogen plasma is not necessary, but a gentle exposure with low temperature is enough to clean the surface.

200 L oxidation of a flashed Si surface at $400\,^{\circ}\mathrm{C}$ created an oxide on the surface. STM measurements showed visible two-dimensional islands on the surface indicating local crystalline order despite local variation. Heating the surface to $600\,^{\circ}\mathrm{C}$ increased the surface roughness.

RCA cleaned Si surface had a chemically grown oxide on the surface and did not provide any LEED pattern prior to UHV annealing. Annealing at $500\,^{\circ}\mathrm{C}$ didn't result a LEED pattern, but $700\,^{\circ}\mathrm{C}$ resulted a faint (1x1). The band gap measured with STS was the same for both $500\,^{\circ}\mathrm{C}$ and $700\,^{\circ}\mathrm{C}$ annealed samples, indicating that the surface was still clearly oxidized after $700\,^{\circ}\mathrm{C}$ annealing. The reason for the (1x1) diffraction spots could be the contribution of the underlying bulk layers due to the increased roughness which makes the oxide layer thinner, or that annealing increases the crystalline order of the oxide. Annealing in $800\,^{\circ}\mathrm{C}$ changed the surface structure to (2x1)(1x2) reconstruction, but STM showed that the surface roughness had increased, highlighting that LEED isn't an absolute measure of surface crystallinity. An increase to $800\,^{\circ}\mathrm{C}$ was also crucial for the surface oxygen concentration reduction, as the O 1s showed a 30-time decrease in XPS.

Oxidation of native oxide covered Si diode sidewalls increased the oxide concentration at the surface. Additionally, the electron levels in the band gap near the Fermi levels decreased, which lead to lower leakage current in the reverse bias voltage region. The resulted oxide has proven to be stable as re-measuring the leakage current after 1 year showed only a very slight increase in the leakage current. This gives a good reason for UHV based treatments to be included in the silicon device fabrication process.

List of References

[1] Chris A. Mack. Fifty Years of Moore's Law. *IEEE Transactions on Semiconductor Manufacturing*, 24(2):202–207, May 2011.

[2] Ruge Quhe, Lin Xu, Shiqi Liu, Chen Yang, Yangyang Wang, Hong Li, Jie Yang, Qiuhui Li, Bowen Shi, Ying Li, Yuanyuan Pan, Xiaotian Sun, Jingzhen Li, Mouyi Weng, Han Zhang, Ying Guo, Linqiang Xu, Hao Tang, Jichao Dong, Jinbo Yang, Zhiyong Zhang, Ming Lei, Feng Pan, and Jing Lu. Sub-10 nm two-dimensional transistors: Theory and experiment. *Physics Reports*, 938:1–72, November 2021.

[3] Dan Zhang, Shujuan Mao, Guilei Wang, Jing Xu, Xue Luo, Chao Zhao, Junfeng Li, Wenwu Wang, Dapeng Chen, Tianchun Ye, and Jun Luo. Exploration of the impact of interface states density on the specific contact resistivity in TiSi $_x$ /n$^+$ -Si Ohmic contacts through high-low frequency method. *Japanese Journal of Applied Physics*, 58(SH):SHHD01, July 2019.

[4] Jimmy Melskens, Bas W. H. Van De Loo, Bart Macco, Lachlan E. Black, Sjoerd Smit, and W. M. M. Kessels. Passivating Contacts for Crystalline Silicon Solar Cells: From Concepts and Materials to Prospects. *IEEE Journal of Photovoltaics*, 8(2):373–388, March 2018.

[5] Charles Kittel. *Introduction to solid state physics*. Wiley, Hoboken, NJ, 8th edition, 2005.

[6] Neil W. Ashcroft and David N. Mermin. *Solid state physics*. HRW international editions. Saunders, Philadelphia, 1976.

[7] Ben G. Streetman and Sanjay Banerjee. *Solid state electronic devices*. Pearson, Boston, 7th edition, 2015.

[8] Viktor Håkansson Inger via Wikimedia Commons. File:Diamond cubic crystal structure.svg, January 2016. URL `https://commons.wikimedia.org/wiki/File:Diamond_cubic_crystal_structure.svg`. CC-BY-SA-4.0, Accessed: 17.11.2025.

[9] Manijeh Razeghi. *Fundamentals of solid state engineering*. Springer, New York, 2nd edition, 2006.

[10] User:Solid_State via Wikimedia Commons. File:GaN Wurtzite polyhedra.png, April 2008. URL `https://commons.wikimedia.org/wiki/File:GaN_Wurtzite_polyhedra.png`. CC-BY-SA-4.0, Accessed: 17.11.2025.

[11] John Singleton. *Band theory and electronic properties of solids*. Oxford University Press, Oxford, 1st edition, 2012.

[12] Safa Kasap and Peter Capper, editors. *Springer Handbook of Electronic and Photonic Materials*. Springer Handbooks. Springer International Publishing, Cham, 2017.

[13] Marius Grundmann. *The Physics of Semiconductors: An Introduction Including Nanophysics and Applications*. Graduate Texts in Physics. Springer International Publishing, Cham, 2016. ISBN 978-3-319-23879-1 978-3-319-23880-7. doi: 10.1007/978-3-319-23880-7.

[14] User:Cepheiden via Wikimedia Commons. File:Band structure Si schematic.svg, September 2008. URL `https://commons.wikimedia.org/wiki/File:Band_structure_Si_schematic.svg`. CC-BY-SA 2.5, Accessed: 25.11.2025.

[15] M. B. Barbosa, J. G. Correia, K. Lorenz, R. Vianden, and J. P. Araújo. Studying electronic properties in GaN without electrical contacts using y-y vs. e–y Perturbed Angular Correlations. *Scientific Reports*, 9(1):15734, October 2019. Licence: http://creativecommons.org/licenses/by/4.0/.

[16] Massimo Rudan. *Physics of Semiconductor Devices*. Springer New York, New York, NY, 2015.

[17] Kazuya Masu and Shuhei Amakawa. *Elementary semiconductor device physics : understanding energy band formation using circuit theory*. CRC Press, Boca Raton, 2025.

[18] Giuseppe Greco, Ferdinando Iucolano, and Fabrizio Roccaforte. Ohmic contacts to Gallium Nitride materials. *Applied Surface Science*, 383:324–345, October 2016.

[19] Shuji Nakamura, Naruhito Iwasa, Masayuki Senoh Masayuki Senoh, and Takashi Mukai Takashi Mukai. Hole Compensation Mechanism of P-Type GaN Films. *Japanese Journal of Applied Physics*, 31(5R):1258, May 1992.

[20] Peter Kozodoy, Huili Xing, Steven P. DenBaars, Umesh K. Mishra, A. Saxler, R. Perrin, S. Elhamri, and W. C. Mitchel. Heavy doping effects in Mg-doped GaN. *Journal of Applied Physics*, 87(4):1832–1835, February 2000.

[21] M. J. Deen and P. K. Basu. *Silicon photonics : fundamentals and devices*. Wiley Series in Materials for Electronic & Optoelectronic Applications. Wiley, Chichester, West Sussex, UK ;, 1st edition, 2012.

[22] Veikko Lindroos. *Handbook of silicon based MEMS materials and technologies*. Micro & nano technologies. William Andrew/Elsevier, Amsterdam ;, 1st edition, 2010.

[23] Hai-Peng Ren, Zi-Xuan Zhou, and Celso Grebogi. Nonlinear dynamics in the flexible shaft rotating–lifting system of silicon crystal puller using Czochralski method. *Nonlinear Dynamics*, 102 (2):771–784, October 2020.

[24] Sheng S. Li. *Semiconductor Physical Electronics*. Springer New York, New York, NY, 2nd edition, 2006.

[25] L. Liu and J.H. Edgar. Substrates for gallium nitride epitaxy. *Materials Science and Engineering: R: Reports*, 37(3):61–127, April 2002.

[26] Ander Udabe, Igor Baraia-Etxaburu, and David Garrido Diez. Gallium Nitride Power Devices: A State of the Art Review. *IEEE Access*, 11:48628–48650, 2023.

[27] Steven P. DenBaars, Daniel Feezell, Katheryn Kelchner, Siddha Pimputkar, Chi-Chen Pan, Chia-Chen Yen, Shinichi Tanaka, Yuji Zhao, Nathan Pfaff, Robert Farrell, Mike Iza, Stacia Keller, Umesh Mishra, James S. Speck, and Shuji Nakamura. Development of gallium-nitride-based light-emitting diodes (LEDs) and laser diodes for energy-efficient lighting and displays. *Acta Materialia*, 61(3):945–951, February 2013.

[28] Matteo Meneghini, Gaudenzio Meneghesso, and Enrico Zanoni, editors. *Power GaN Devices: Materials, Applications and Reliability*. Power Electronics and Power Systems. Springer International Publishing, Cham, 2017.

[29] Corsin Battaglia, Katalin Gaál-Nagy, Claude Monney, Clément Didiot, Eike Fabian Schwier, Michael Gunnar Garnier, Giovanni Onida, and Philipp Aebi. Elementary structural building blocks encountered in silicon surface reconstructions. *Journal of Physics: Condensed Matter*, 21(1):013001, January 2009.

[30] Klaus Hermann. *Crystallography and surface structure : an introduction for surface scientists and nanoscientists*. THEi Wiley ebooks. Wiley-VCH, Weinheim, Germany, 2nd edition, 2017.

[31] Harald Ibach. *Physics of Surfaces and Interfaces*. Springer Nature, Berlin, Heidelberg, 1st edition, 2006.

[32] Friedhelm. Bechstedt. *Principles of surface physics*. Advanced texts in physics. Springer, Berlin, 2003.

[33] Zahra Jahanshah Rad, Juha-Pekka Lehtiö, Iris Mack, Kawa Rosta, Kexun Chen, Ville Vähänissi, Marko Punkkinen, Risto Punkkinen, Hannu-Pekka Hedman, Andrei Pavlov, Mikhail Kuzmin, Hele Savin, Pekka Laukkanen, and Kalevi Kokko. Decreasing Interface Defect Densities via Silicon Oxide Passivation at Temperatures Below 450 °C. *ACS Applied Materials & Interfaces*, 12(41):46933–46941, October 2020.

[34] Feng Tao and S. L. Bernasek. *Functionalization of semiconductor surfaces*. Wiley, Hoboken, N.J, 1st edition, 2012.

[35] Takeshi Hattori, editor. *Ultraclean Surface Processing of Silicon Wafers*. Springer Berlin Heidelberg, Berlin, Heidelberg, 1998.

[36] Robert M. Wallace and Glen D. Wilk. High-k Dielectric Materials for Microelectronics. *Critical Reviews in Solid State and Materials Sciences*, 28(4):231–285, October 2003.

[37] M. Morita, T. Ohmi, E. Hasegawa, M. Kawakami, and M. Ohwada. Growth of native oxide on a silicon surface. *Journal of Applied Physics*, 68(3):1272–1281, August 1990.

[38] Werner Kern. Overview and Evolution of Silicon Wafer Cleaning Technology. In *Handbook of Silicon Wafer Cleaning Technology*, pages 3–85. Elsevier, 2018.

[39] Shuichi Sato, Shinji Kawaji, and Akio Kobayashi. Electrical properties of surface states on silicon surfaces. *Surface Science*, 4(3):299–312, May 1966.

[40] David E. Aspnes and Paul Handler. Surface states on cleaved (111) silicon surfaces. *Surface science*, 4(4):353–380, 1966.

[41] Takuo Sugano. Atomically controlled surface and interface, and semiconductor device performance. *Applied Surface Science*, 60-61:698–701, January 1992.

[42] Faiz Rahman, Richard K. Oxland, and Ali Z. Khokhar. Surface passivation of nitride- and phosphide-based compound semiconductors. *Journal of Optoelectronics and Advanced Materials*, 11(8):1117 – 1121, 2009.

[43] Fandi Oktasendra, Rahmat Hidayat, and Rizky Indra Utama. Effects of interface state density on the carrier transport and performance of metal-insulator-semiconductor (MIS) type thin film solar cells. *Journal of Physics: Conference Series*, 1481(1):012005, March 2020.

[44] Sang Hee Lee, Muhammad Fahad Bhopal, Doo Won Lee, and Soo Hong Lee. Review of advanced hydrogen passivation for high efficient crystalline silicon solar cells. *Materials Science in Semiconductor Processing*, 79:66–73, June 2018.

[45] I. Martin, M. Vetter, A. Orpella, C. Voz, J. Puigdollers, R. Alcubilla, A. V. Kharchenko, and P. Roca I Cabarrocas. Improvement of crystalline silicon surface passivation by hydrogen plasma treatment. *Applied Physics Letters*, 84(9):1474–1476, March 2004.

[46] W Henrion, M Rebien, H Angermann, and A Röseler. Spectroscopic investigations of hydrogen termination, oxide coverage, roughness, and surface state density of silicon during native oxidation in air. *Applied Surface Science*, 202(3-4):199–205, December 2002.

[47] Roel J. Theeuwes, Wilhelmus M. M. Kessels, and Bart Macco. Surface passivation approaches for silicon, germanium, and III–V semiconductors. *Journal of Vacuum Science & Technology A*, 42(6):060801, December 2024.

[48] Dieter K. Schroder. *Semiconductor Material and Device Characterization*. Wiley, 1st edition, October 2005.

[49] S. M. Sze and Kwok K. Ng. *Physics of semiconductor devices*. John Wiley & Sons Inc., Hoboken, N.J, 3rd edition, 2007.

[50] R. T. Tung. Electron transport at metal-semiconductor interfaces: General theory. *Physical Review B*, 45(23):13509–13523, June 1992.

[51] W Monch. On the physics of metal-semiconductor interfaces. *Reports on Progress in Physics*, 53 (3):221–278, March 1990.

[52] F. Roccaforte, F. Giannazzo, F. Iucolano, J. Eriksson, M.H. Weng, and V. Raineri. Surface and interface issues in wide band gap semiconductor electronics. *Applied Surface Science*, 256(19): 5727–5735, July 2010.

[53] Keye Sun, Daehwan Jung, Chen Shang, Alan Liu, Jesse Morgan, Jizhao Zang, Qinglong Li, Jonathan Klamkin, John E. Bowers, and Andreas Beling. Low dark current III–V on silicon photodiodes by heteroepitaxy. *Optics Express*, 26(10):13605, May 2018.

[54] Mitsuru Takenaka, Kiyohito Morii, Masakazu Sugiyama, Yoshiaki Nakano, and Shinichi Takagi. Dark current reduction of Ge photodetector by GeO_2 surface passivation and gas-phase doping. *Optics Express*, 20(8):8718, April 2012.

[55] Hiroaki Tanaka, Tatsunori Isogai, Tetsuya Goto, Akinobu Teramoto, Shigetoshi Sugawa, and Tadahiro Ohmi. Low Contact Resistivity with Low Silicide/p^+ -Silicon Schottky Barrier for High-Performance p-Channel Metal–Oxide–Silicon Field Effect Transistors. *Japanese Journal of Applied Physics*, 49(4S):04DA03, April 2010.

[56] Heinrich Häberlin. *Photovoltaics: System Design and Practice*. John Wiley & Sons Inc., 1st edition, February 2012.

[57] Takeo Oku. *Solar cells and energy materials*. Walter de Gruyter, GmbH, Berlin ;, 1st edition, 2017. ISBN 978-3-11-038106-1.

[58] Joachim N. Burghartz and IEEE Electron Devices Society. *Guide to state-of-the-art electron devices*. Wiley - IEEE. John Wiley & Sons Inc., Chichester, West Sussex, U.K, 1st edition, 2013.

[59] Nagamitsu Yoshimura, editor. *Vacuum Technology: Practice for Scientific Instruments*. Springer-Link Bücher. Springer-Verlag Berlin Heidelberg, Berlin, Heidelberg, 2008.

[60] Neil T. Peacock. Chapter 4.2 - Flange and Component Systems. In *Handbook of Vacuum Science and Technology*, pages 409–432. Elsevier Inc, 1998.

[61] Dorothy M. Hoffman, Bawa. Singh, and John H. Thomas. *Handbook of vacuum science and technology*. Academic Press, San Diego, CA, 1st edition, 1998.

[62] K. Jousten. *Handbook of vacuum technology*. Wiley-VCH Verlag GmbH & Co. KGaA, Weinheim, Germany, 2nd edition, 2016.

[63] Paul Van der Heide. *X-ray photoelectron spectroscopy : an introduction to principles and practices*. Wiley, Hoboken, N.J, 2012.

[64] Mauro Sardela. *Practical materials characterization*. Springer, New York, NY, 2014.

[65] J. C. Vickerman and Ian S. Gilmore, editors. *Surface analysis: the principal techniques*. Wiley, Chichester, U.K, 2nd edition, 2009.

[66] John Moudler, William Stickle, Peter Sobol, and Kenneth Bomben. *Handbook of X-ray Photoelectron Spectroscopy*. Perkin-Elmer Corporation, October 1992.

[67] Phil Willmott. *An introduction to synchrotron radiation: techniques and applications*. Wiley, Chichester, West Sussex, U.K, 1st edition, 2011.

[68] Phil Woodruff. *Surface Science and synchrotron radiation*. IOP Ebooks Series. IOP Publishing, Bristol, England, 1st edition, 2023.

[69] R. Pärna, R. Sankari, E. Kukk, E. Nõmmiste, M. Valden, M. Lastusaari, K. Kooser, K. Kokko, M. Hirsimäki, S. Urpelainen, P. Turunen, A. Kivimäki, V. Pankratov, L. Reisberg, F. Hennies, H. Tarawneh, R. Nyholm, and M. Huttula. FinEstBeaMS – A wide-range Finnish-Estonian Beamline for Materials Science at the 1.5 GeV storage ring at the MAX IV Laboratory. *Nuclear Instruments and Methods in Physics Research Section A: Accelerators, Spectrometers, Detectors and Associated Equipment*, 859:83–89, July 2017.

[70] Kirill Chernenko, Antti Kivimäki, Rainer Pärna, Weimin Wang, Rami Sankari, Mats Leandersson, Hamed Tarawneh, Vladimir Pankratov, Mati Kook, Edwin Kukk, Liis Reisberg, Samuli Urpelainen, Tanel Käämbre, Frank Siewert, Grzegorz Gwalt, Andrey Sokolov, Stephanie Lemke, Svyatoslav Alimov, Jeniffa Knedel, Oliver Kutz, Tino Seliger, Mika Valden, Mika Hirsimäki, Marco Kirm, and Marko Huttula. Performance and characterization of the FinEstBeAMS beamline at the MAX IV Laboratory. *Journal of Synchrotron Radiation*, 28(5):1620–1630, September 2021.

[71] F. Jona, J. A. Strozier Jr, and W. S. Yang. Low-energy electron diffraction for surface structure analysis. *Reports on Progress in Physics*, 45(5):527, May 1982.

[72] G. Binnig, H. Rohrer, Ch. Gerber, and E. Weibel. Surface Studies by Scanning Tunneling Microscopy. *Physical Review Letters*, 49(1):57–61, July 1982.

[73] Rebecca S. Howland and Michael D. Kirk. 2.3 - STM and SFM: Scanning Tunneling Microscopy and Scanning Force Microscopy. In C. Ricbard Brundle, Charles A. Evans, and Shaun Wilson, editors, *Encyclopedia of Materials Characterization*, pages 85–98. Butterworth-Heinemann, Boston, 1992.

[74] J. Tersoff and N. D. Lang. 1 - Theory of scanning tunneling microscopy. In Joseph A. Stroscio and William J. Kaiser, editors, *Scanning Tunneling Microscopy*, pages 1–29. Academic Press, San Diego, 1993.

[75] C. Julian Chen. *Introduction to scanning tunneling microscopy*. Monographs on the physics and chemistry of materials. Oxford University Press, Oxford, England, 3rd edition, 2021.

[76] R M Feenstra and Joseph A Stroscio. Real-Space Determination of Surface Structure by Scanning Tunneling Microscopy. *Physica Scripta*, T19A:55–60, January 1987.

[77] Andrew H. Simon. Chapter 3 - Sputter processing. In Dominic Schepis and Krishna Seshan, editors, *Handbook of Thin Film Deposition (Fifth Edition)*, pages 93–140. Elsevier, 5th edition, 2025.

TURUN
YLIOPISTO
UNIVERSITY
OF TURKU

ISBN 978-952-02-0555-3 (PRINT)
ISBN 978-952-02-0556-0 (PDF)
ISSN 0082-7002 (PRINT)
ISSN 2343-3175 (ONLINE)

Painosalama, Turku, Finland 2026